

University of Nebraska - Lincoln

DigitalCommons@University of Nebraska - Lincoln

Faculty Publications, Department of Physics and
Astronomy

Research Papers in Physics and Astronomy

2017

A Decade of H α Transits for HD 189733 b: Stellar Activity versus Absorption in the Extended Atmosphere

P. Wilson Cauley

Seth Redfield

Adam G. Jensen

Follow this and additional works at: <https://digitalcommons.unl.edu/physicsfacpub>

This Article is brought to you for free and open access by the Research Papers in Physics and Astronomy at DigitalCommons@University of Nebraska - Lincoln. It has been accepted for inclusion in Faculty Publications, Department of Physics and Astronomy by an authorized administrator of DigitalCommons@University of Nebraska - Lincoln.



A Decade of $H\alpha$ Transits for HD 189733 b: Stellar Activity versus Absorption in the Extended Atmosphere

P. Wilson Cauley¹, Seth Redfield¹, and Adam G. Jensen²

¹ Wesleyan University, Astronomy Department, Van Vleck Observatory, 96 Foss Hill Drive, Middletown, CT 06459, USA; pcauley@wesleyan.edu

² University of Nebraska-Kearney, Department of Physics & Astronomy, 24011 11th Avenue, Kearney, NE 68849, USA

Received 2017 January 11; revised 2017 March 24; accepted 2017 March 27; published 2017 April 18

Abstract

HD 189733 b is one of the most well studied exoplanets due to its large transit depth and host star brightness. The focus on this object has produced a number of high-cadence transit observations using high-resolution optical spectrographs. Here we present an analysis of seven full $H\alpha$ transits of HD 189733 b using HARPS on the 3.6 meter La Silla telescope and HIRES on Keck I, taken over the course of nine years from 2006 to 2015. $H\alpha$ transmission signals are analyzed as a function of the stellar activity level, as measured using the normalized core flux of the Ca II H and K lines. We find strong variations in the strength of the $H\alpha$ transmission spectrum from epoch to epoch. However, there is no clear trend between the Ca II core emission and the strength of the in-transit $H\alpha$ signal, although the transit showing the largest absorption value also occurs when the star is the most active. We present simulations of the in-transit contrast effect and find that the planet must consistently transit active latitudes with very strong facular and plage emission regions in order to reproduce the observed line strengths. We also investigate the measured velocity centroids with models of planetary rotation and show that the small line profile velocities could be due to large velocities in the upper atmosphere of the planet. Overall, we find it more likely that the measured $H\alpha$ signals arise in the extended planetary atmosphere, although a better understanding of active region emission for active stars such as HD 189733 is needed.

Key words: planets and satellites: atmospheres – planets and satellites: individual (HD 189733 b) – stars: activity – stars: individual (HD 189733) – techniques: spectroscopic

1. Introduction

Hot planets, or planets orbiting within ~ 10 stellar radii of their host stars and which have orbital periods of a few days, are unique subjects for planetary astrophysics. The extreme proximity to their host stars can result in phenomena that are not observable in other exoplanet systems (for a recent review of these processes, see Matsakos et al. 2015). These phenomena include atmospheric mass loss (e.g., Vidal-Madjar et al. 2003; Murray-Clay et al. 2009; Ehrenreich et al. 2012, 2015; Bourrier et al. 2013; Khodachenko et al. 2016; Salz et al. 2016), magnetic and tidal star–planet interactions (e.g., Cuntz et al. 2000; Shkolnik et al. 2008; Lanza 2009; Poppenhaeger & Wolk 2014; Strugarek et al. 2014; Miller et al. 2015; Pillitteri et al. 2015), and bow shocks that can form where the planet’s atmosphere or magnetosphere plows through the stellar wind (e.g., Lai et al. 2010; Llama et al. 2011, 2013; Vidotto et al. 2011; Ben-Jaffel & Ballester 2013; Cauley et al. 2015; Turner et al. 2016). Due to the larger magnitude of the potentially observable effect, giant hot planets ($M \gtrsim M_{\text{Neptune}}$) are particularly good targets for investigating these processes.

One of the most well studied hot Jupiters is HD 189733 b (Bouchy et al. 2005). Due to the brightness of its host star ($V = 7.7$) and its large transit depth ($\sim 2.4\%$), HD 189733 b has been the target of many detailed observing campaigns over the last decade (see Section 1.2 of Bourrier et al. 2013 for a recent overview). One of the most exciting results was the observation of evaporating material by Lecavelier des Etangs et al. (2010), who measured a 5% transit depth at $\text{Ly}\alpha$ and concluded that the absorbing material must be gravitationally unbound. A follow-up study showed that the evaporation is highly variable: no absorption was detected in a set of 2010

$\text{Ly}\alpha$ observations while a strong $\text{Ly}\alpha$ transit, with absorption up to $\sim 14\%$ measured in the blue wing of the line profile, was detected in 2011 (Lecavelier des Etangs et al. 2012). These results were the first indication of variability in the mass loss of a hot exoplanet.

Evaporation of hot planets is driven by atmospheric heating from the absorption of X-ray and extreme UV (EUV) stellar radiation (e.g., Murray-Clay et al. 2009; Owen & Jackson 2012). Two mechanisms can thus produce variations in the amount of X-ray and EUV flux received by a hot planet: (1) stellar rotation and the planet’s orbital motion, which cause active regions³ of differing strengths to be directed toward the planet throughout its orbit; (2) intrinsic time variability in the stellar activity level due to long-term activity cycles or short-term variability, such as flares. These variations provide a natural explanation for changes in the planetary evaporation rate and suggest that hot planets subjected to larger amounts of ionizing stellar radiation will have higher evaporation rates (Owen & Adams 2016).

Measuring the exospheres of hot planets requires space-based UV observations (e.g., Fossati et al. 2010; Ben-Jaffel & Ballester 2013; Bourrier et al. 2013). However, the extended atmosphere, or the thermosphere at pressures of 10^{-6} – 10^{-9} bar, can be observed from the ground using the neutral hydrogen Balmer line transitions (Jensen et al. 2012; Astudillo-Defru & Rojo 2013; Christie et al. 2013; Cauley et al. 2015, 2016). The first $H\alpha$ detection was made by Jensen et al. (2012). Christie et al. (2013) modeled the Jensen et al. (2012) detection and showed that the strength of $H\alpha$ absorption in the atmosphere of a hot Jupiter is dependent on the amount of

³ Throughout the paper we refer to active regions as portions of the stellar surface covered by spots or faculae and plages.

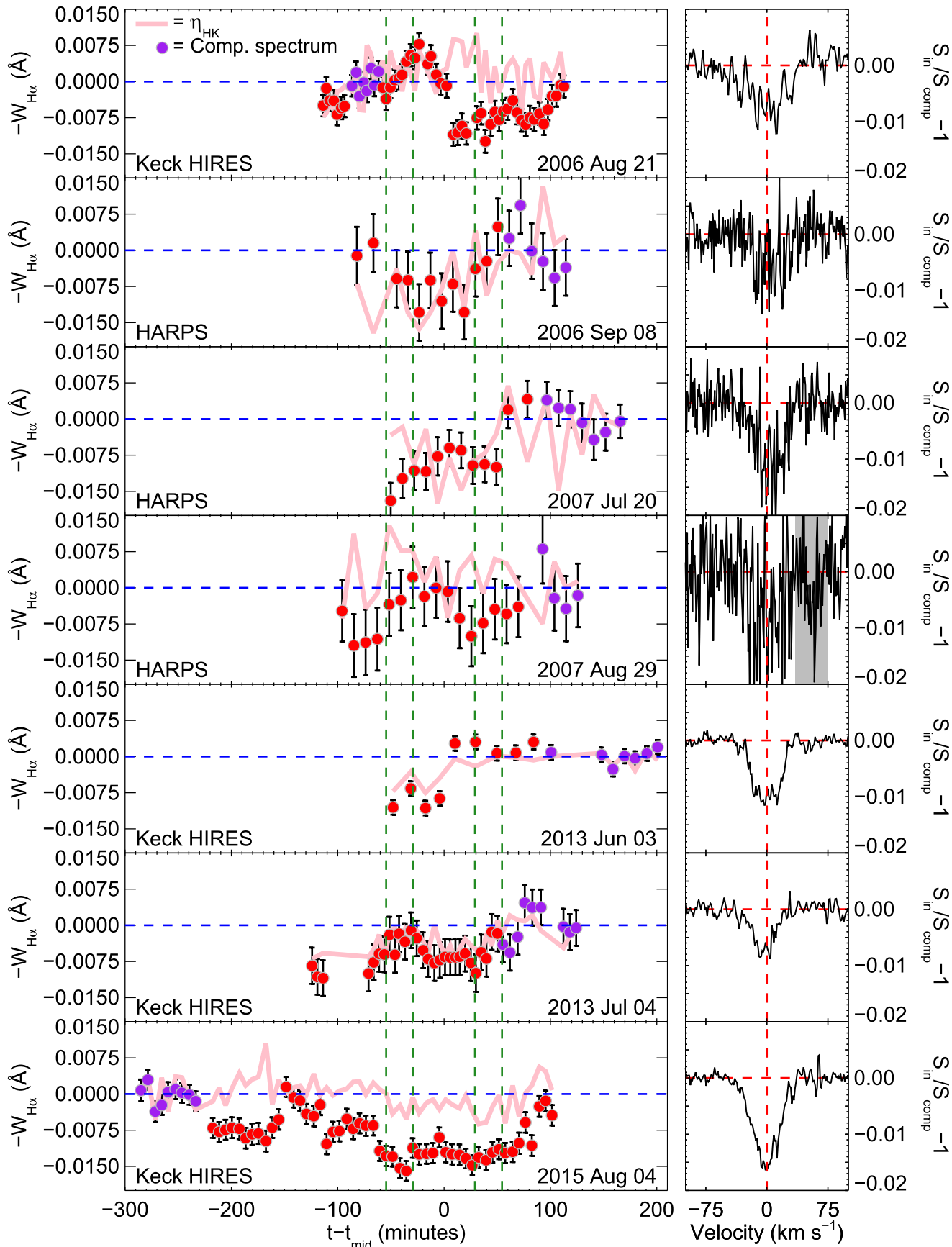


Figure 1. $H\alpha$ absorption time-series for the seven dates from Table 1. The $W_{H\alpha}$ points are shown with red circles. Observations used as comparison spectra are shown as purple circles. All dates are shown on the same scale. The thick pink line shows the scaled and median-corrected η_{HK} values in order to convey how the Ca II flux changes correlate with changes in $W_{H\alpha}$. The right column shows the master in-transit transmission spectrum for each transit. Note that only observations showing 1σ absorption are included in the master transmission spectrum.

Table 1
Archived Data Sets

UT Date (1)	Instrument (2)	Program ID (3)	N_{obs} (4)	N_{used} (5)	S/N @ 6571 Å (6)	R (7)	$\lambda_{\text{start}}, \lambda_{\text{end}}$ (8)
2006 Aug 21	Keck HIRES	A259Hr	70	55	230	49,000	3360 Å, 7800 Å
2006 Sep 8	HARPS	072.C-0488(E)	18	18	149	115,000	3800 Å, 6800 Å
2007 Jul 20	HARPS	079.C-0828(A)	39	39	140	115,000	3800 Å, 6800 Å
2007 Aug 29	HARPS	079.C-0127(A)	40	40	131	115,000	3800 Å, 6800 Å
2013 Jun 3	Keck HIRES	A308Hr	17	16	440	68,000	3500 Å, 7400 Å
2013 Jul 4	Keck HIRES	A308Hr	40	37	490	68,000	3500 Å, 7400 Å
2015 Aug 4	Keck HIRES	N120Hr	61	61	490	68,000	3500 Å, 7400 Å

ionizing stellar radiation, with larger amounts of radiation producing stronger absorption. Thus while $H\alpha$ observations most likely do not directly probe the evaporating material, the strength of absorption in the extended atmosphere may provide insight into the strength of the evaporation.

Recently, Barnes et al. (2016) used archival HARPS data to measure in-transit $H\alpha$ transmission spectra for HD 189733 b across three separate transits. Based on velocity maps of the absorption signatures in both the stellar and planetary rest frames, the authors point out that the absorption signal moves from redshifted to blueshifted velocities in the planetary rest frame and shows no velocity gradient across the transit in the stellar rest frame. They suggest that this is evidence of the absorption signature arising in the frame of the star, i.e., it is not absorption by planetary material but rather the result of continuum-to-line contrast effects that arise as the planet occults different portions of the stellar disk. They also highlight the potential problems with using continuum-to-line differential measurements for chromospherically sensitive lines: a non-uniform stellar surface with active regions can be weighted toward a stronger or weaker line core based on which portion of the stellar surface is occulted by the planet, resulting in a contrast effect between the line core and nearby continuum region (Berta et al. 2011). Barnes et al. (2016) conclude that the transit signatures measured in the chromospherically sensitive lines, in particular $H\alpha$ and the Ca II H and K lines, are the result of the contrast effect and not due to absorption by planetary material. This is especially relevant to active stars such as HD 189733 ($S_{\text{HK}} = 0.52$; compared to the solar value of $S_{\text{HK}} = 0.17$; Wright et al. 2004).

In this paper we examine seven archival transits of HD 189733 b, including the same HARPS data analyzed by Barnes et al. (2016), in order to search for a relationship between the stellar activity level and the strength of the in-transit $H\alpha$ signal. We do not include the results of Jensen et al. (2012) since these observations were not performed across a single transit. We produce detailed transit models to investigate the contrast effect and determine if the $H\alpha$ signatures measured by Jensen et al. (2012), Cauley et al. (2015, 2016), and Barnes et al. (2016) can be attributed to occultation of a non-uniform stellar surface rather than absorption by planetary material. We also discuss how planetary rotation can affect the measured absorption velocities, which we calculate for each transit, and present transmission spectrum models of rotation in an extended planetary atmosphere. The investigation into the absorption line velocities is motivated by the suggestion of Barnes et al. (2016) that the $H\alpha$ transmission is not due to the planetary atmosphere. Their main argument is that the $H\alpha$ line velocities do not follow the pattern expected from absorption in the

Table 2
 $H\alpha$ Absorption and η_{HK} Values

UT Date (1)	$W_{H\alpha}$ ^a (10^{-3} Å) (2)	Mean In-transit $-\eta_{\text{HK}}$ ^b (Å) (3)	Mean Comparison $-\eta_{\text{HK}}$ (Å) (4)
2006 Aug 21	9.11 ± 0.94	0.373 ± 0.019	0.370 ± 0.025
2006 Sep 8	9.29 ± 1.10	0.358 ± 0.046	0.424 ± 0.043
2007 Jul 20	10.00 ± 1.07	0.246 ± 0.043	0.291 ± 0.056
2007 Aug 29	7.89 ± 2.30	0.299 ± 0.050	0.245 ± 0.075
2013 Jun 3	9.14 ± 0.32	0.389 ± 0.011	0.415 ± 0.008
2013 Jul 4	6.84 ± 0.42	0.346 ± 0.014	0.364 ± 0.013
2015 Aug 4	12.80 ± 0.45	0.540 ± 0.013	0.558 ± 0.025

Notes.

^a Uncertainties are calculated by propagating the flux uncertainty for each spectrum through Equation (2).

^b Uncertainties are the standard deviation of the points included in the mean.

planetary atmosphere, although we note that they do not present quantitative measurements of the line velocities. The data sets and reduction processes are described in Section 2. The transmission spectrum is defined in Section 3 and the average $H\alpha$ transmission spectra are given. $H\alpha$ and Ca II H and K time-series measurements are presented in Section 4 for each transit. Section 5 includes an examination of epoch-to-epoch changes in $H\alpha$ absorption and the stellar activity level as measured using the Ca II H and K lines. The contrast models are discussed in Section 6 and the atmospheric rotation models and measured line velocities are given in Section 7. Section 8 provides a brief summary and conclusion of our results.

2. Observations and Data Reduction

The observations presented here are a combination of HD 189733 b transits observed with HARPS (Mayor et al. 2003) on the 3.6 m telescope at La Silla and HIRES (Vogt et al. 1994) on Keck I. Information about each data set is detailed in Table 1, including the average signal-to-noise ratio (S/N) of an individual exposure in the continuum near 6571 Å. All data are currently available on either the ESO data archive or the Keck Observatory Archive. The archive ID for each data set is given in Table 1. We note that the HARPS data are the same as used by Wyttenbach et al. (2015) and Louden & Wheatley (2015) to study Na I absorption in HD 189733 b's atmosphere. The Keck data from 2006 August 21 are the same data used to

measure the Rossiter–McLaughlin effect for HD 189733 b by Winn et al. (2006). We also retrieved an archival transit obtained using UVES (Dekker et al. 2000) by Czesla et al. (2015) to study center-to-limb variations of the Na I D lines. This transit, however, is fundamentally different when compared to all of the other H α transits and does not match any of the features seen in the HIRES and HARPS time series. This abnormal behavior is due to the mid-transit flare identified by Czesla et al. (2015). Finally, we exclude archival transits from the High Dispersion Spectrograph on Subaru due to the lack of simultaneous Ca II observations.

HARPS has a resolving power of $R \sim 115,000$ and the HIRES observations were performed at $R \sim 49,000$ using the B5 decker and $R \sim 68,000$ using the B2 decker. The reduced HARPS data were taken directly from the ESO archive. Note that we do not perform the scattered light removal process described by Barnes et al. (2016). We believe that a comparison of our time-series results and average transmission spectra provide justification: we obtain almost identical results for the behavior of both H α and Ca II using the standard HARPS reduction routines.

Standard reduction steps including bias subtraction, flat fielding, and wavelength calibration were performed for the Keck data using the publicly available HIRES Redux program by Jason X. Prochaska.⁴ All spectra are shifted to the rest frame of the star by correcting for the Earth’s barycentric velocity and HD 189733’s system radial velocity, for which we use the mean value -2.23 km s^{-1} from Di Gloria et al. (2015).

We used the latest version of Molecfit (Kausch et al. 2014) in order to model telluric absorption in the H α order. We first construct a master telluric model by using a telluric standard observed on the same night. The master telluric model is then fit to a selection of telluric lines in the individual science exposures using a χ^2 minimization routine. We fit for the line depth, small wavelength shifts, and line broadening. The best-fit scaled, broadened, and shifted telluric model is then divided out of the normalized science spectrum. This routine works very well for most spectra, removing the telluric absorption down to 5%–10% of the original line depth. This typically results in transmission spectrum residuals of $\sim 0.1\%$ – 0.5% near the cores of the telluric lines. Due to the low S/N, we were unable to adequately remove the telluric absorption immediately redward of H α for the 2007 August 29 observations (see Figure 1). This portion of the spectrum is not included in the absorption calculations.

Two-element wavelength binning is applied to all of the individual HARPS spectra in order to increase the S/N. We also co-add back-to-back spectra from the nights of 2007 July 20 and August 29 due to the short exposure times (300 s). Note that the S/N values for the HARPS spectra in Table 1 are calculated for the co-added and binned spectra. The individual Keck observations required no binning. Some spectra near the beginning or end of the night are not included in the analysis due to $S/N \lesssim 50$ or contamination by Earth’s twilight sky spectrum.

3. Transmission Spectra

The transmission spectrum is defined here as:

$$S_T = \frac{F_i}{F_{\text{out}}} - 1 \quad (1)$$

where F_i is a single in-transit observation and F_{out} is the master comparison spectrum. To produce the final transmission spectra, we apply the same wavelength alignment and normalization procedures described in Cauley et al. (2015, 2016). The comparison spectra are generally chosen to be those taken furthest from the transit, although there is no strict rule for doing so, and their number is selected to minimize the impact of any single spectrum while not using too many of the available observations as comparison exposures. For example, the 2006 August 21 comparison spectra are chosen as those immediately before the transit in order to balance the low $W_{\text{H}\alpha}$ values near $t - t_{\text{mid}} = -100$ min and the increase in $W_{\text{H}\alpha}$ immediately after the transit begins. The choice of comparison spectra can significantly influence the absolute level of measured absorption but the relative changes between observations remain the same. For this study, the choice of out-of-transit comparison spectra does not significantly change the results for any of the transits except the 2015 August 4 data. The choice of comparison spectra for 2015 August 4 is detailed in Cauley et al. (2016).

The average H α in-transit transmission spectrum for the individual transits is shown in the rightmost column of Figure 1. Only individual in-transit observations showing 1σ significant absorption are selected to be included in the average transmission spectra in order to highlight the line morphology. Including all of the in-transit observations from 2013 June 3, for example, results in a much weaker transmission spectrum due to the abrupt decrease in absorption mid-transit. Master absorption measurements (see Equation (2)) are given for each date in Table 2. Absorption is detected at the 3σ level for all transits.

Significant variations in S_T from epoch to epoch are evident, especially in the high-S/N Keck spectra. The HARPS spectra are fairly noisy but clear changes in line depth, and even shape, can be seen. These variations suggest that if the signal arises in HD 189733 b’s extended planetary atmosphere, it changes rather drastically from one epoch to the next, and perhaps within individual epochs, as observed in the Ly α exosphere by Lecavelier des Etangs et al. (2010, 2012) and across the multiple H α transits observed by Jensen et al. (2012).

4. Time-series H α Absorption and the Normalized Ca II Core Flux

For each individual spectrum we calculate the following absorption measure, essentially an equivalent width of the transmission spectrum, at H α :

$$W_{\text{H}\alpha} = \sum_{v=-200}^{+200} \left(1 - \frac{F_v}{F_v^{\text{out}}} \right) \Delta\lambda_v \quad (2)$$

where F_v is the flux in the spectrum of interest at velocity v , F_v^{out} is the flux in the comparison spectrum at velocity v , and $\Delta\lambda_v$ is the wavelength difference at velocity v . The units of $W_{\text{H}\alpha}$ are angstroms. The gray shaded region in the transmission spectrum for 2007 August 29 is ignored due to poor telluric subtraction.

Individual HARPS transmission spectra are normalized across the $\pm 200 \text{ km s}^{-1}$ region by averaging the fits of a line and a low-order spline. The $\pm 40 \text{ km s}^{-1}$ at line center are ignored in the normalization. Individual Keck spectra, which have much higher S/N than the HARPS transmission spectra

⁴ <http://www.ucolick.org/~xavier/HIRedux/>

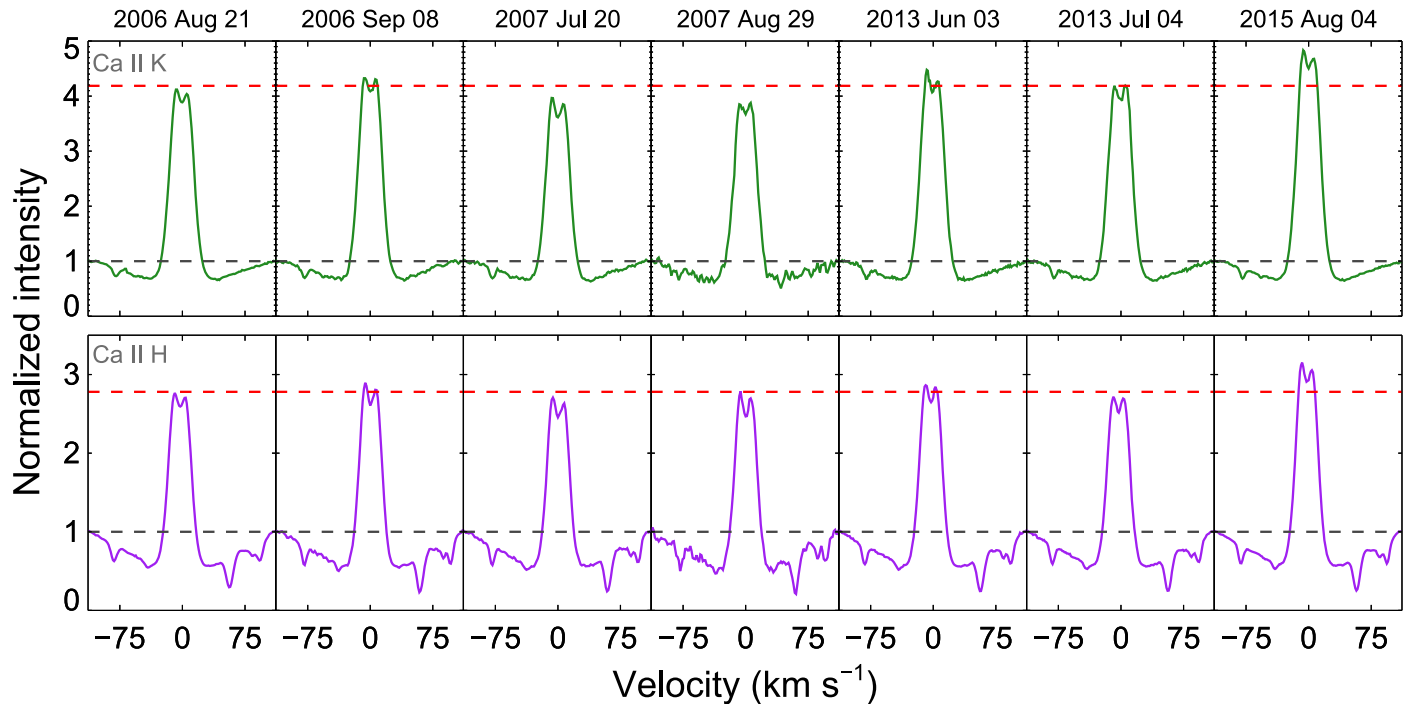


Figure 2. Normalized mean Ca II H and K profiles for the comparison spectra from each date. The dashed charcoal line shows the normalization level and the dashed red line shows the median maximum flux level for all dates. Note the strong excess core emission for 2015 August 4.

and have fewer telluric residuals, require only a second-order polynomial to adequately remove the continuum slope. We note that small residual offsets from zero in the normalized HARPS transmission spectra can result in $W_{H\alpha}$ offsets of ~ 0.001 Å. These residuals, however, are also present in the $W_{H\alpha}$ values calculated for the individual comparison points. For this reason, we do not separately include the normalization uncertainties.

We derive uncertainties in $W_{H\alpha}$ by combining in quadrature two different sources of uncertainty. First, normalized flux errors in the transmission spectrum are summed in quadrature. This is then added in quadrature to the standard deviation of the comparison spectra $W_{H\alpha}$ points (purple circles in Figure 1). The standard deviation uncertainties dominate the normalized flux uncertainties in most cases. We note that this is different from the empirical Monte Carlo (EMC) procedure used in Redfield et al. (2008), Jensen et al. (2012), and Cauley et al. (2015, 2016) but has a similar outcome: large variations in the comparison spectra, like in the 2013 July 4 transit, will produce larger uncertainties in all of the individual points. We choose to use the standard deviation of the comparison points since the HARPS time series, compared with the 2013 and 2015 Keck time series, have relatively fewer comparison spectra ($N = 4-7$ compared to $N = 8$ for the 2013 and 2015 Keck nights). The EMC procedure becomes less useful with smaller numbers of comparison spectra. The standard deviation uncertainties are ~ 2.6 times greater than the EMC uncertainties for the individual 2013 and 2015 Keck data points. This is approximately equal to \sqrt{N} where N is the number of comparison spectra used. We recommend that future studies adopt the more conservative standard deviation estimate for individual time series points.

In order to test for correlations between the stellar activity level and $W_{H\alpha}$, we define the following measure of the average

between the Ca II H and K core fluxes:

$$\eta_{HK} = \frac{1}{2} \left[\sum (F_N^H - 1) \Delta\lambda_H + \sum (F_N^K - 1) \Delta\lambda_K \right] \quad (3)$$

where F_N^H is the core flux of the Ca II H line normalized to the 0.1 Å wide regions centered at ± 1.5 Å from the rest wavelength of the line. $\Delta\lambda_H$ is the dispersion near Ca II H and the flux integration is done between $\lambda_0^H \pm 1.5$ Å. The symbols have the same meaning for Ca II K. Note that we do not perform the residual Ca II H and K core analysis from Cauley et al. (2016) due to the low S/N of the HARPS spectrum. The η_{HK} measures essentially the same thing but information about the shape of the residual line profile is lost. In-transit and comparison spectra η_{HK} values are given in Table 2. The mean Ca II H and K profiles for the comparison observations are shown in Figure 2. The median maximum normalized flux is marked with a red dashed line.

Figure 1 shows $W_{H\alpha}$ (red circles) as a function of the time from mid-transit for each of the transits listed in Table 1. All rows are on the same vertical and horizontal scale. The thick pink lines show a scaled value of η_{HK} that has been shifted by the median η_{HK} value of the comparison spectra (purple circles). The vertical green lines show the transit contact points and the horizontal blue line marks $W_{H\alpha} = 0.0$. Consistent transits in $H\alpha$ are detected for the HARPS data on 2006 September 8 and 2007 July 20. Transits showing transient absorption signatures are detected for 2006 August 21, 2007 August 29, and 2013 June 3. The shape of the $W_{H\alpha}$ HARPS timeseries measurements are very similar to those presented by Barnes et al. (2016).

A few things are immediately evident from Figure 1. First, the $H\alpha$ signal is highly variable, showing large deviations from

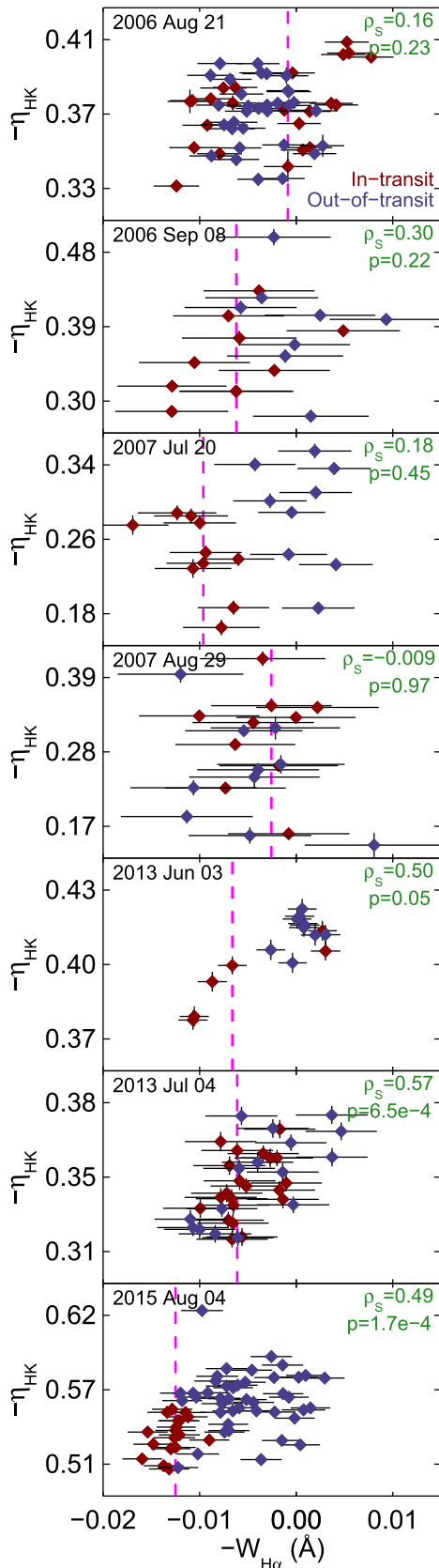


Figure 3. Correlation plots between $W_{H\alpha}$ and η_{HK} . In-transit points are shown in dark red and out-of-transit points are shown in dark blue. The median in-transit $W_{H\alpha}$ value is marked with a vertical magenta dashed line. Correlations significant at the 99% level are present for 2007 July 20 and 2013 July 4.

epoch to epoch in both the strength of the absorption and in the duration of the transit. Second, the data from 2006 August 21, 2007 August 29, and 2013 June 3 show abrupt in-transit changes in $W_{H\alpha}$. This contrasts with the other four dates which show fairly uniform in-transit absorption that is typical of, for example, a non-varying extended atmosphere. Lastly, 2006 August 21, 2013 July 4, and 2015 August 4 show evidence of absorption outside of the optical transit times: 2006 August 21 shows post-transit absorption, 2013 July 4 shows pre-transit absorption, and 2015 August 4 shows both pre- and post-transit absorption. The pre-transit signals from 2013 July 4 and 2015 August 4 have been explored in Cauley et al. (2015, 2016). The abrupt in-transit changes could be due to transits of active regions on the stellar surface or varying levels of stellar activity. Active region transits will be investigated in Section 6 and correlations with the Ca II H and K lines will be discussed in the next subsection.

4.1. Stellar Activity versus Planetary Absorption

As discussed in Cauley et al. (2015, 2016), changes in stellar activity from one observation to another can mimic absorption by circumplanetary material. We note that this is separate from the in-transit contrast effect, which is discussed in Section 6. One method of distinguishing absorption from stellar variability is to compare the $W_{H\alpha}$ values with simultaneous measurements of an independent measure of the stellar activity level. Changes in $W_{H\alpha}$ can be more confidently attributed to absorption if there is no correlation with the independent stellar activity measure.

Figure 3 shows the values of $W_{H\alpha}$ versus η_{HK} for each epoch. In-transit observations are shown in dark red while out-of-transit observations are shown in dark blue. We calculate Spearman's ρ rank correlation coefficients for each date. The ρ_s value and corresponding two-sided significance p are shown in green in the upper-right of each panel. Only the dates of 2013 June 3, 2013 July 4, and 2015 August 4 show significant ($p \lesssim 0.05$) correlations between $W_{H\alpha}$ and η_{HK} . The 2015 August 4 correlation is largely driven by the distinct in- and out-of-transit groupings, i.e., there is no correlation within the in-transit points or within the out-of-transit points. The clumping of the points from 2013 June 3 likely prevents the correlation from being stronger but η_{HK} clearly changes at the same time as $W_{H\alpha}$ near $t - t_{mid} = 0$ min. We discuss the relationship between $W_{H\alpha}$ and η_{HK} for the uniform $W_{H\alpha}$ transits in the next section.

For the non-uniform transits of 2006 August 21, 2007 August 29, and 2013 June 3, the interpretation of the η_{HK} and $W_{H\alpha}$ relationship is uncertain. The small number of comparison points and low S/N of the 2007 August 29 data make this transit especially difficult to interpret. The 2006 August 21 and 2013 June 3 transits both feature abrupt changes in $W_{H\alpha}$ at mid-transit, producing strong absorption in the case of 2006 August 21 and filling in the absorption in the case of 2013 June 3. The clear change in η_{HK} at a similar time in the 2013 June 3 transit suggests that this may be entirely attributable to changes in the stellar activity level. This is not the case for 2006 August 21.

It seems unlikely that such abrupt changes can be due to physical variations in the planetary atmosphere. However, transiting gas (e.g., previously evaporated material) not associated with the atmosphere could cause such changes. In this case, the atmosphere would show no absorption and the

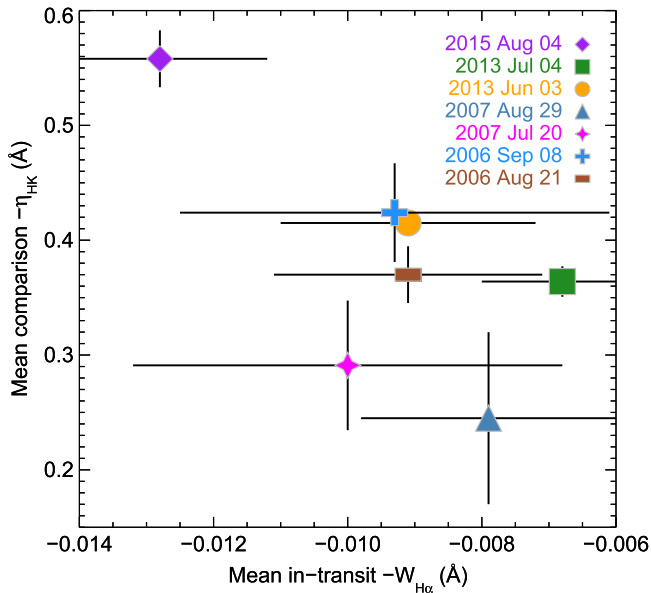


Figure 4. Comparison between the mean in-transit values of $W_{H\alpha}$ and $-\eta_{HK}$ calculated for the mean Ca II H and K comparison spectra shown in Figure 2. Uncertainties in η_{HK} for 2013 June 3 are smaller than the size of the plot symbol. There is no clear trend. However, the date with the highest η_{HK} by a large margin is 2015 August 4 (purple) and this date also shows the deepest and most extended $H\alpha$ transit, suggesting that the extended atmosphere is strongly influenced by the stellar activity level if the $H\alpha$ signal arises in the planetary atmosphere.

external feature (e.g., a condensation or accretion stream; Lai et al. 2010; Lanza 2014) would be orbiting ahead of the planet in the case of 2013 June 3 and behind the planet for the 2006 August 21 data. The feature would have to be $\sim 5 R_p$ ahead of or behind HD 189733 b for the transit to end or begin halfway through the planet’s transit. Although it is unclear as to the exact nature of these short-term $W_{H\alpha}$ variations, which are present in all of the transits, we showed in Cauley et al. (2017) that changes of the magnitudes seen, for example, in the 2013 June 3 and 2006 August 21 data, are rare when the planet is out-of-transit, suggesting that they occur preferentially when the planet is in- or near-transit. We find it more likely that these changes are due to variable absorption in the circumplanetary environment since stochastic changes in the stellar activity level, as a result of star–planet interactions, should be observable at orbital phases not associated with the transit.

4.2. Ca II as an Absorber

Although Ca II emission is a widely examined indicator of chromospheric activity, it is possible that Ca II atoms in the extended atmosphere of HD 189733 b might have enough opacity to absorb stellar photons (Turner et al. 2016). Lanza (2014) posited that Ca II absorption in stellar prominences fed by planetary mass loss could be responsible for the correlation between planetary surface gravity and $\log R'_{HK}$ found by Hartman (2010) (see also Fossati et al. 2015). Indeed, detections of multiple transitions of neutral calcium have been claimed in the atmosphere of HD 209458 b (Astudillo-Defru & Rojo 2013). If there is significant Ca II absorption by the planet, the measured in-transit core flux is no longer directly tracing the short-term stellar activity level, especially when comparing in-transit to out-of-transit observations. This is hinted at by the fact that five of seven transits have lower mean in-transit η_{HK} values compared to the comparison spectrum η_{HK} value

Table 3
Stellar and Planetary Parameters

Parameter (1)	Symbol (2)	Value ^a (3)	Units (4)
Stellar radius	R_*	0.756	R_\odot
Stellar rotational velocity	$v \sin i$	3.10	km s^{-1}
Impact parameters	b	0.680	R_*
Orbital period	P_{orb}	2.218573	days
Orbital velocity	v_{orb}	151.96	km s^{-1}
Orbital semimajor axis	a	0.03099	au
Planetary radius	R_p	1.138	R_J

Note.

^a With the exception of $v \sin i$, all stellar and planetary parameters taken from Torres et al. (2008). The $v \sin i$ value is taken from Collier Cameron et al. (2010).

Table 4
Contrast Model Parameters and Explored Values

Parameter Description (1)	Symbol (2)	Value Range (3)
Spot coverage fraction	A_{sp}	0.005–0.10
Ratio of spots to faculae	Q	2.0–0.2
Filament coverage fraction	A_{fil}	0.005–0.03
Ratio of facular to photosphere core $H\alpha$	q_{fac}	0.1–6.0
FWHM of facular emission	σ_{fac}	10–50 km s^{-1}
Central latitude of active region distribution	θ_{act}	0° – 45°
Temperature difference between spots and photosphere	ΔT_{sp}	300–800 K
Temperature difference between faculae and photosphere	ΔT_{fac}	20–50 K
Filament $H\alpha$ core contrast	c_{fil}	0.2–0.8
Minimum spot radius	$r_{\text{sp}}^{\text{min}}$	0.1 – $0.5 R_p$
Maximum spot radius	$r_{\text{sp}}^{\text{max}}$	0.3 – $1.0 R_p$

(see Table 2). We note, however, that the probability of measuring a decrease in η_{HK} in at least five of the seven transits is $\sim 22\%$, assuming that there is an equal probability of measuring either an increase or decrease. Thus we cannot say with any statistical certainty that the in-transit Ca II measurements show a preference for absorption. Increasing the number of transits at Ca II would help clarify whether the observed statistics are representative of a real effect.

Planetary Ca II absorption may explain the data for the dates showing lower in-transit $-\eta_{HK}$ values and fairly smooth $W_{H\alpha}$ transits. For the 2006 September 8, 2007 July 20, 2013 July 4, and 2015 August 4 transits the mean η_{HK} value for the comparison spectra is more negative (meaning more core flux) than the mean in-transit η_{HK} value. We find significant correlations between $W_{H\alpha}$ and η_{HK} for 2013 July 4 and 2015 August 4. The 2013 July 4 correlation is driven by a correlation *within* the out-of-transit points ($\rho_S = 0.71$, $p = 0.002$); none of the other dates shows correlations within only the in- or out-of-transit points. However, the 2013 July 4 out-of-transit correlation is itself driven by strong differences between the pre-transit points and the post-transit comparison points (see Figure 1). Thus we do not see strong evidence of correlated changes between $W_{H\alpha}$ and η_{HK} from one exposure to another. This tentatively suggests that the lower in-transit η_{HK} differences are not due to changes in the stellar activity level.

An alternative to absorption in the planetary atmosphere producing the lower in-transit η_{HK} values is the transiting of bright active regions (Llama & Shkolnik 2015). If the planet happens to transit an especially active latitudinal band that is bright in Ca II compared to the rest of the star, the Ca II core emission will be preferentially blocked by the planet's disk, resulting in lower in-transit η_{HK} values. Unless the active latitude is fairly uniform in brightness, the transit tends to be choppy and uneven (Llama & Shkolnik 2015). Although the Ca II light curves in Figure 1 do show some significant exposure-to-exposure variations, the epochs with lower in-transit versus out-of-transit η_{HK} values (e.g., 2007 July 20 and 2013 July 4) exhibit fairly smooth time series. Thus we tentatively favor the atmospheric absorption scenario over active region transits, although a thorough investigation of the contrast effect at Ca II H and K would be informative.

If Ca II in the planetary atmosphere is indeed absorbing, it cannot be considered a reliable independent measure of the stellar activity level near (i.e., immediately pre- or post-transit) or during the planet's transit. Detailed theoretical modeling of the Ca II population in the extended atmospheres of hot exoplanets would be useful in determining whether Ca II should be specifically targeted in these systems. A possible alternative is simultaneous monitoring of FUV activity diagnostics (e.g., France et al. 2016) that are not expected to be present in the extended atmospheres of hot planets.

5. Epoch-to-epoch Variations

The significant exospheric changes measured in Ly α by Lecavelier des Etangs et al. (2012) and Bourrier et al. (2013) for HD 189733 b motivates us to look for changes in the H α signal as a function of stellar activity level. This has also been investigated previously by Barnes et al. (2016) for the HARPS transits. Christie et al. (2013) showed that the strength of H α planetary absorption depends strongly on the Ly α and ionizing flux from the star. In order to match the strength of H α absorption measured by Jensen et al. (2012), Christie et al. (2013) find that a large value of the ionizing flux is needed. For reference, the H α absorption measured by Jensen et al. (2012) is comparable to that measured for the 2015 August 4 transit. This result suggests that dates showing larger values of out-of-transit η_{HK} should show larger amounts of in-transit H α absorption.

The strongest core emission in Figure 2 is clearly seen for 2015 August 4. Figure 4 shows the mean $-\eta_{\text{HK}}$ value from Figure 2 plotted against the mean in-transit $-W_{\text{H}\alpha}$ from each date. The uncertainty in each value is the standard deviation of the points included in the mean value. Only points showing 1σ significant absorption are included in the mean $W_{\text{H}\alpha}$ values.

There is no clear trend between $W_{\text{H}\alpha}$ and η_{HK} from epoch to epoch. However, 2015 August 4 stands out: it shows the strongest in-transit H α absorption signal and the largest out-of-transit η_{HK} value. In addition, the 2015 August 4 H α transit appears significantly extended both pre- and post-transit, hinting at an atmosphere that fills a significant fraction of the planet's Roche lobe. The low H β and H γ absorption values from Cauley et al. (2016) also support the presence of a low-density extended atmosphere. This suggests that there may be some threshold (e.g., $-\eta_{\text{HK}} \gtrsim 0.40$) for the stellar activity level below which the extended atmosphere is fairly uniform and constant. We note that the in- versus out-of-transit differences in η_{HK} within a single night are much less than the inter-epoch

variations. Thus although we have argued that Ca II may be absorbing stellar photons around the planet, we do not expect the absorption effect to be as large as night-to-night variations in the stellar activity level, as seen, for example, by Boisse et al. (2009) across many weeks of H α and Ca II observations of HD 189733 and similarly at H α by Cauley et al. (2017).

It is not clear if the star was in a particularly active state during the 2015 August 4 transit or an especially active hemisphere of the star was visible during that night. The suggested threshold needs to be confirmed with a larger sample of transits, ideally during periods when the star is in an especially active state, that show consistent H α absorption since the interpretation of irregular transits (e.g., 2006 August 21 and 2007 August 29) is much less straightforward.

Overall, we find no strong evidence for a relationship between the stellar activity level and the strength of the in-transit $W_{\text{H}\alpha}$ measurement, although the date with the highest η_{HK} value also shows the strongest in-transit H α absorption. The analysis presented here should be supplemented in the future with more transit observations, preferably containing as many simultaneous activity indicators as possible. In the next section, we investigate whether or not the contrast effect for HD 189733 can explain the observed H α absorption signatures. A similar analysis will be presented in a future paper for Ca II, Na I, and Mg I.

6. The Contrast Effect for HD 189733

While much effort has been made to calculate the effects of star spots, faculae and plagues,⁵ and other irregular surface features on stellar radial velocities, broadband transmission spectra, and properties derived from transit measurements (e.g., Saar & Donahue 1997; Aigrain et al. 2012; Dumusque et al. 2014; Oshagh et al. 2014; Andersen & Korhonen 2015; Llama & Shkolnik 2015; Giguere et al. 2016; Herrero et al. 2016; Rackham et al. 2017), little has been published on the details of how these same features affect high-resolution transmission spectra. Berta et al. (2011) and Sing et al. (2011) present analytic approximations for how the broadband transmission spectrum changes as a function of star spot filling factor and temperature. Here we present an investigation into the high-resolution H α contrast effect, i.e., how the ratio of in-transit to out-of-transit flux as a function of wavelength changes based on which portion of the star is being occulted by the planet. This is critical to understanding how the surface of an active star such as HD 189733 will affect the $W_{\text{H}\alpha}$ measurement, especially in light of the recent suggestion by Barnes et al. (2016) that the H α signal is due mostly to variations on the stellar surface and not to absorption by circumplanetary material.

6.1. Model Overview

Here we provide a brief overview of the steps involved in creating the model transmission spectra. The stellar and planetary parameters used in the model are given in Table 3. The model has eleven input parameters which are listed in Table 4 along with the range of parameter values we explored with the contrast model, but most of the examples presented

⁵ We do not distinguish between faculae, which form in the photosphere, and plagues, which form in the chromosphere. The spectra used to model bright H α regions on the stellar surface are a combination of both plague and facular characteristics.

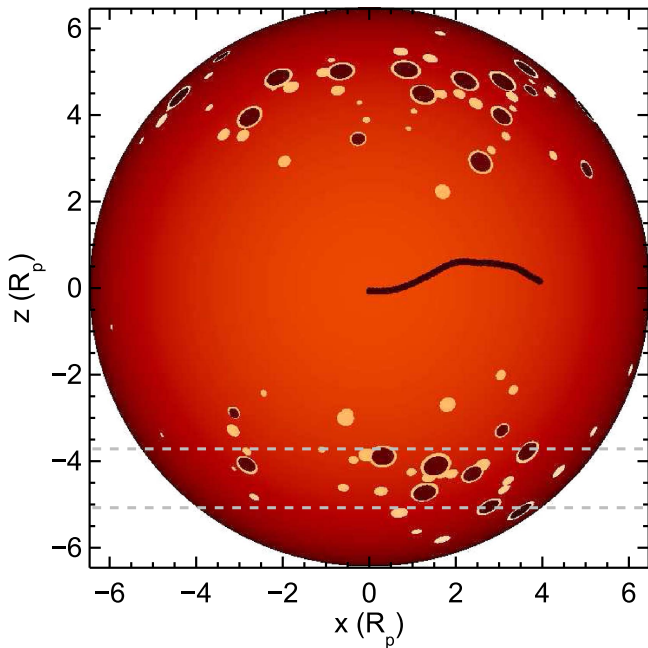


Figure 5. Example stellar disk for a contrast model with $A_{\text{sp}} = 0.02$, $Q = 0.7$, and $A_{\text{fil}} = 0.005$. The faculae are shown as white annuli surrounding the dark brown spots and randomly placed circles with the same latitudinal distribution as the spots. A dark filament can be seen across disk center. The transit path of HD 189733 b is shown by the dashed gray lines. Note that the limb-darkening, and limb-brightening in the case of the faculae, are meant to be representative of how the features contribute near the $H\alpha$ line core (i.e., absorption or emission) and not to show the precise intensity ratios calculated as a function of wavelength in the models.

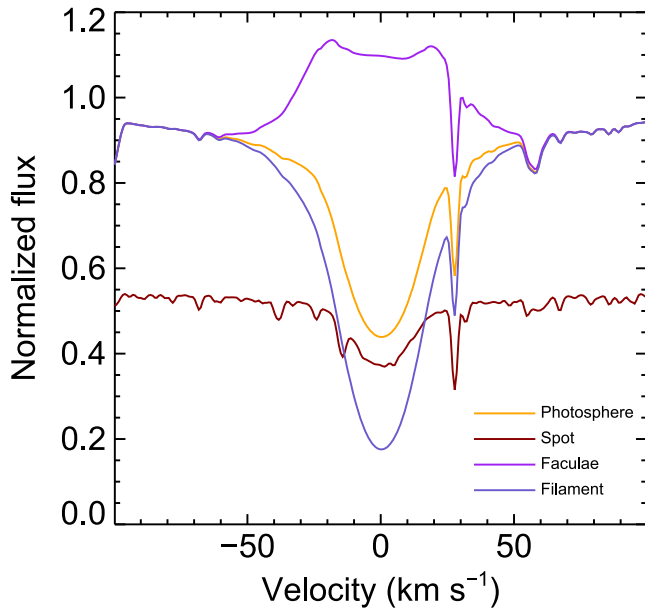


Figure 6. Model surface feature $H\alpha$ spectra at $\mu = 1$ for $T_{\text{sp}} = 4300$ K, $q_{\text{fac}} = 1.5$, $T_{\text{fac}} = 5040$ K, and $c_{\text{fil}} = 0.6$. Each spectrum is normalized by fitting a line to the flux at -200 and $+200$ km s^{-1} . Note that these are spectra of *individual* surface elements and do not represent the absolute fluxes contributing to the explored contrast examples. The core emission in the facular spectrum (purple line) completely fills in the photospheric absorption in this case. We note that this is more typical of a flare rather than a quiescent facular region and is shown here to illustrate the differences between the spectra. The temperature difference between the spot and the photosphere results in $\sim 45\%$ less flux from the spot (dark red line). The filament (dark blue line) shows strong $H\alpha$ core absorption superimposed on the photospheric spectrum. The narrow feature near 30 km s^{-1} is a Cr I line. We ignore the absorption contribution from this line when calculating $W_{H\alpha}$.

below focus on a much smaller range or even specific values. This is due to the fact that some parameters have little influence on the contrast effect.

We first simulate the location of spots and faculae on the stellar disk. We assume that each spot has some concentric associated facular region that has an area equal to 60% of the spot area. After all spot locations have been determined, additional facular regions are added to match the desired spot-to-facular ratio $Q = A_{\text{sp}}/A_{\text{fac}}$. The location of a spot is determined by randomly selecting from a normal distribution in latitude centered on the latitude input parameter. The full width at half maximum (FWHM) of the distribution is kept fixed at 10° . The size of the spot is then determined by randomly selecting from a uniform distribution with boundaries specified by $r_{\text{sp}}^{\text{min}}$ and $r_{\text{sp}}^{\text{max}}$, the minimum and maximum allowed spot radii in units of R_p . We do not allow overlap of spots. Finally, the projected boundaries, which are ellipses, of the spot and surrounding faculae are determined based on the central spot location. The additional facular regions are added in an identical procedure except the edges of the ellipses may overlap to allow potentially more irregular patterns.

We also include filaments which appear in absorption against the stellar disk (e.g., Heinzel & Anzer 2006; Kuckein et al. 2016). The filaments have a fixed width of $0.2 R_p$ and their length is defined by the total filament coverage fraction. Filaments are constructed by choosing a random starting point and direction and then letting the filament grow in that direction with a narrow cone defining the directions in which each new piece of the filament is allowed to move toward. The filament is allowed to grow until the desired coverage fraction is achieved to within 0.1%.

To simulate the transmission spectrum, we first calculate the out-of-transit spectrum by summing the spectra from individual grid points across the entire stellar surface. The grid resolution is $0.02 R_p$ which results in a 647×647 Cartesian grid. The surface feature spectra are PHOENIX model spectra with the addition of a Gaussian emission profile or extinction of the photospheric spectrum, assuming a Gaussian profile shape, depending on the type of feature (e.g., a plage or filament). The emission and absorption profiles are assumed to be Gaussian due to the approximately Gaussian shape of the observed $H\alpha$ transmission spectra. In addition, the exact line shape is less important than the magnitude of the effect, which will not change significantly if a Lorentzian or Voigt profile is assumed. The spectrum at each point on the stellar disk is shifted by the appropriate stellar rotational velocity, for which we assume rigid rotation. We also compute the radial velocity of the star relative to the observer (see Equation (11) of Logis & Fischer 2010) and apply this velocity shift to each of the stellar spectra. We then calculate the stellar spectrum blocked by the planet at five minute intervals across the transit. The out-of-transit spectrum is subtracted from the blocked spectrum and then the result is divided by the out-of-transit spectrum to generate synthetic transmission spectra according to Equation (1). An example of the stellar surface for the parameters $A_{\text{sp}} = 0.02$, $Q = 0.7$, and $A_{\text{fil}} = 0.005$ is shown in Figure 5.

6.2. Surface Feature Spectra

Each distinct surface feature contributes a different $H\alpha$ spectrum. We include four separate surface components: (1) the naked photosphere; (2) star spots; (3) faculae; (4) filaments. Below we discuss each spectrum in detail, as well as the other

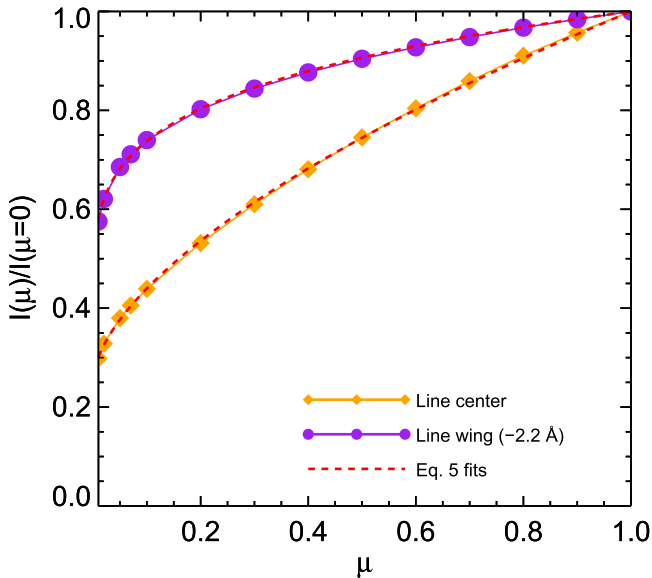


Figure 7. Examples of wavelength-dependent limb-darkening curves from the synthetic spectra (solid lines and symbols) and the fits using Equation (5) (red dashed lines). Note the steeper limb-darkening in the line core compared with the line wing.

parameters associated with that specific surface feature. Example $H\alpha$ spectra of the four surface components at $\mu = \cos \theta = 1.0$, where θ is the angle between the normal vector to the stellar surface and the line-of-sight, are shown in Figure 6 for a model with $T_{\text{sp}} = 4300$ K, $q_{\text{fac}} = 1.5$, $T_{\text{fac}} = 5040$ K, and $c_{\text{fil}} = 0.6$. The faculae are approximately the same brightness as the photosphere at $\mu = 1.0$ (see Equation (4)). The normalized continuum flux for the spot spectrum is reduced by a factor of $(T_{\text{sp}}/T_{\text{eff}})^4$. We ignore all small-scale velocity effects in the spectra, such as photospheric convective blueshifts, since we are only concerned with the overall contrast between the different regions. The contrast is weakly affected by these velocity shifts, which are of the order $\sim 200\text{--}300$ m s^{-1} (e.g., Meunier et al. 2010b; Lanza et al. 2011).

6.2.1. Photospheric Spectra

For the photosphere we use a PHOENIX model spectrum (Husser et al. 2013) with $T_{\text{eff}} = 5000$ K, $\log g = 4.5$, and $[\text{Fe}/\text{H}] = 0.0$. It is important to emphasize that the choice of photospheric spectrum is not critical to exploring the contrast effect since most of the stellar surface is dominated by the photosphere. Furthermore, the spotted, filament, and facular spectra are scaled by or built from the photospheric spectrum in some manner so the entire surface is constructed relative to the photosphere. Thus a choice of the model T_{eff} of 4500 K or 5500 K does not significantly affect our conclusions. We note that Boyajian et al. (2015) recently measured T_{eff} for HD 189733 to be 125 K lower (4875 ± 43 K) than the value used here.

6.2.2. Spot Spectra

For the star spot spectra we use PHOENIX model spectra with the same $\log g$ and $[\text{Fe}/\text{H}]$ values but with varying temperatures in step sizes of 100 K. Spots are cooler than the surrounding photosphere with differences in temperature that depend on spectral type, although this dependence may break down at $T_{\text{eff}} > T_{\odot}$ (Eker et al. 2003; Berdyugina 2005). Note that we do not distinguish between umbral and penumbral

temperatures; they are averaged into a single spot temperature. Herrero et al. (2016) demonstrate (their Figure 2) the good agreement between observed solar spot spectra and model PHOENIX spectra at a cooler T_{eff} .

Pont et al. (2013) provided a detailed analysis of spot-crossing events during HD 189733 b transits. Their main conclusions were: (1) there is no evidence for the transiting of concentrated bright faculae, suggesting that facular regions are spread out across the stellar surface; (2) the spot filling factor is $\sim 1\%$ – 2% ; (3) the temperature difference between the photosphere and spots is $\Delta T = 750$ K. Photometric modeling performed by Herrero et al. (2016) suggests that spots dominate changes in the stellar brightness across stellar rotation periods. The observations presented in Pont et al. (2013) span ~ 6 yr, which provides evidence that the spot filling factor does not change significantly on long timescales. Their results provide reasonable spot parameter values around which to base our investigation.

6.2.3. Filament Spectra

Filament spectra are identical to photospheric spectra but with the $H\alpha$ line core subject to further absorption. Kuckein et al. (2016) measure the contrast across $H\alpha$ from ~ -80 to $+80$ km s^{-1} for filaments on the solar disk. They find $\sim 60\%$ less flux in the line core compared with the bare photosphere, although the values vary depending on where the measurement is made on the filament. We adopt a single contrast value of 0.6 (i.e., 60% less flux) at the line core for the filament spectra. The absorption is modeled as a Gaussian with a FWHM of 40 km s^{-1} . We do not consider prominences, which are filaments projected beyond the edge of the stellar disk, although large prominences may produce pre- or post-transit contrast signals.

6.2.4. Facular Spectra

Facular spectra consist of the intensity-weighted sum of the underlying photosphere and overlying emission region. During small solar flares, the ratio of $H\alpha$ line core emission to the underlying photospheric spectrum can reach $\sim 2.0\text{--}4.0$ (Johns-Krull et al. 1997; Xu et al. 2016). The ratios measured for non-flaring faculae are closer to ~ 1.2 (Ahn et al. 2014) and very weak flares show ratios of $\sim 1.1\text{--}1.6$, or $q_{\text{fac}} = 0.1\text{--}0.6$ (Deng et al. 2013). For the contrast models, we are only interested in the low-level stellar activity that does not change dramatically over the course of a single night. This implies values for $q_{\text{fac}} \sim 0.1\text{--}2.0$. Larger ratios than this likely do not apply to non-flaring regions. However, we explore larger values of q_{fac} since larger values are needed to reproduce the observed $W_{H\alpha}$ values. Whether or not these large values for the $H\alpha$ core emission are physical will be discussed below.

Facular and plage regions are limb-brightened relative to the underlying photosphere. We adopt the limb-brightening law of Meunier et al. (2010a) and Herrero et al. (2016):

$$c_{\text{fac}}(\mu) = \left(\frac{T_{\text{eff}} + \Delta T(\mu)}{T_{\text{eff}} + \Delta T_{\text{fac}}} \right)^4 \quad (4)$$

where ΔT_{fac} is the temperature difference between the photosphere and faculae and $\Delta T(\mu) = 250.9 - 407.4\mu + 190.9\mu^2$.

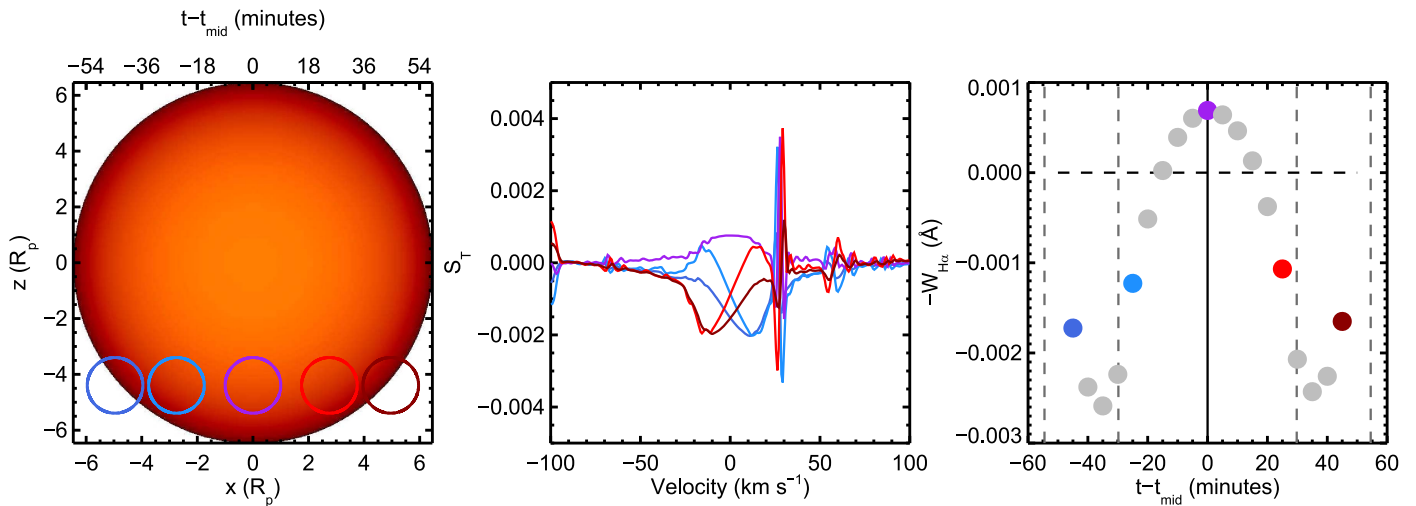


Figure 8. Example of the contrast effect for a star with no spots, faculae, or filaments. The planet’s position at five in-transit times is shown with the solid circles (left panel). The top x -axis gives the time from mid-transit corresponding to the distances on the bottom x -axis. The transmission spectra S_T for each in-transit time are shown in the middle panel. The narrow spikes near 27 km s^{-1} are the result of a Cr I line at 6563.40 \AA . Note that this line is ignored in the calculation of $W_{H\alpha}$. S_T shows a shift from stronger to weaker absorption as the planet approaches mid-transit. This is the result of CLVs where the difference between the limb-darkening in the wing vs. the line core is smallest near the middle of the stellar disk. Note the difference in scale between the right panel and the transmission spectra shown in Figure 1. The CLV effects are an order of magnitude lower than the measured signals. The right panel shows the $W_{H\alpha}$ values calculated for the full set of in-transit times. The vertical dashed lines mark the transit contact points and the vertical solid line marks mid-transit. The strongest absorption signal, or in this case contrast signal, is when the planet is near the edge of the stellar disk but still almost completely covers the limb. This is very similar behavior to the Na I D calculations presented by Czesla et al. (2015).

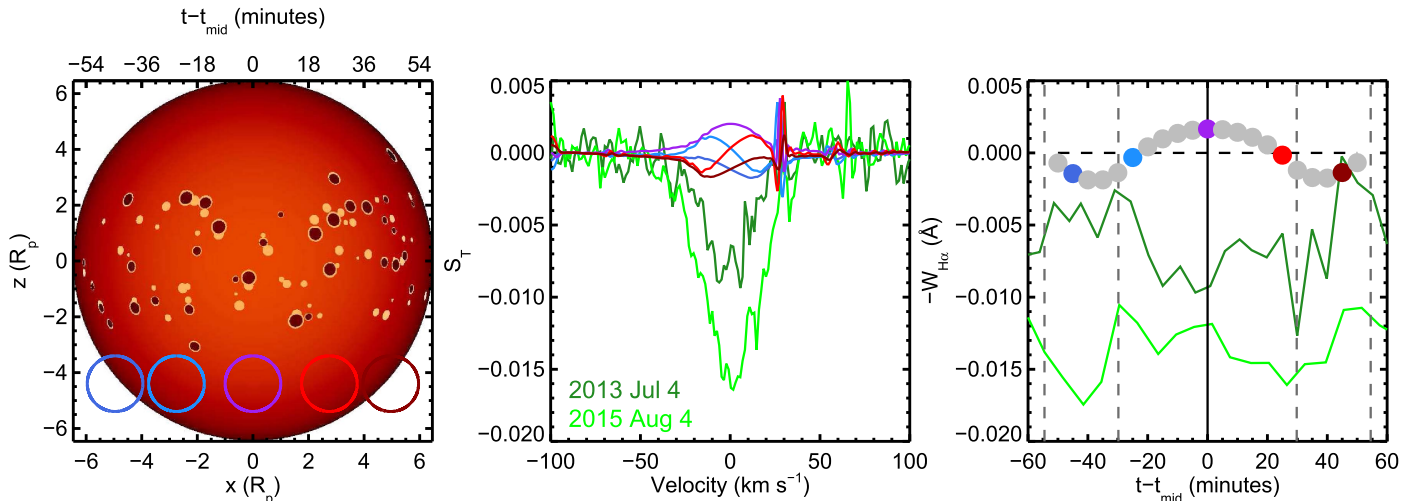


Figure 9. Transit of a photospheric chord with $A_{sp} = 0.02$, $Q = 0.7$, $A_{fil} = 0.0$, $\theta_{act} = \pm 10^\circ$, and $q_{fac} = 1.5$. The 2013 July 4 and 2015 August 4 Keck data are shown in green in both the middle and right panels. Note the different scale compared with Figure 8. Since the in-transit spectrum is weighted toward the active regions, the $W_{H\alpha}$ curve (right panel) is shifted up due to the line core being filled in by facular emission. This can also be seen in S_T (middle panel) where the spectra show stronger emission features.

6.3. Contrast and Limb-darkening/brightening

Czesla et al. (2015) calculated differential center-to-limb variations (CLVs), or differences in the limb-darkening or brightening as a function of wavelength across a specific spectral line, for the Ca II H and K and Na I D lines for HD 189733. They demonstrated that the Na I lines show limb-brightening in the wings of the line compared with the line core or neighboring continuum. This is important since a transiting planet with no atmosphere can produce a transmission signal, even if there are no active regions present on the stellar surface, due to the fact that the ratio of the line core to the continuum

changes as a function of the transit (see Figures 1–5 of Czesla et al. 2015). This effect was recently included in Na I transit modeling by Khalafinejad et al. (2017).

Such CLVs will also affect the in-transit $H\alpha$ measurements. In order to account for this effect, we have calculated high-resolution $H\alpha$ spectra using the program SPECTRUM⁶ by Gray & Corbally (1994) and an ATLAS9 model atmosphere⁷ with $T_{\text{eff}} = 5000 \text{ K}$, $\log g = 4.5$, and $[\text{Fe}/\text{H}] = 0.0$. The spectra

⁶ <http://www.appstate.edu/~grayro/spectrum/spectrum.html>

⁷ <http://wwwuser.oats.inaf.it/castelli/>

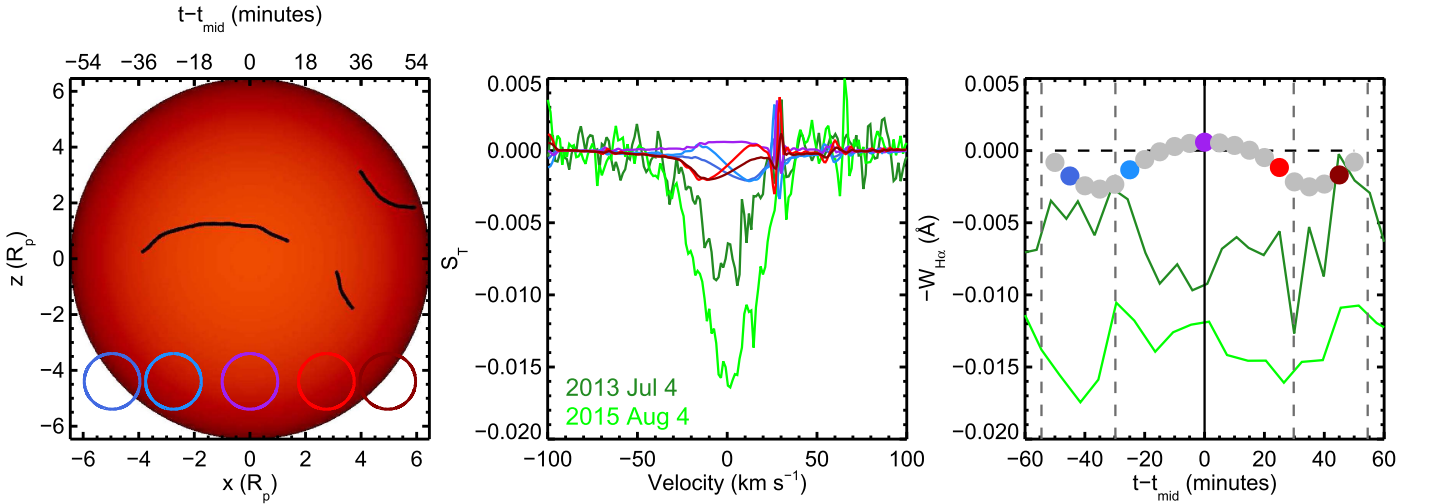


Figure 10. Same as Figure 9 but for the pure filament case with $A_{\text{fil}} = 0.01$. The filaments produce a very weak contrast effect.

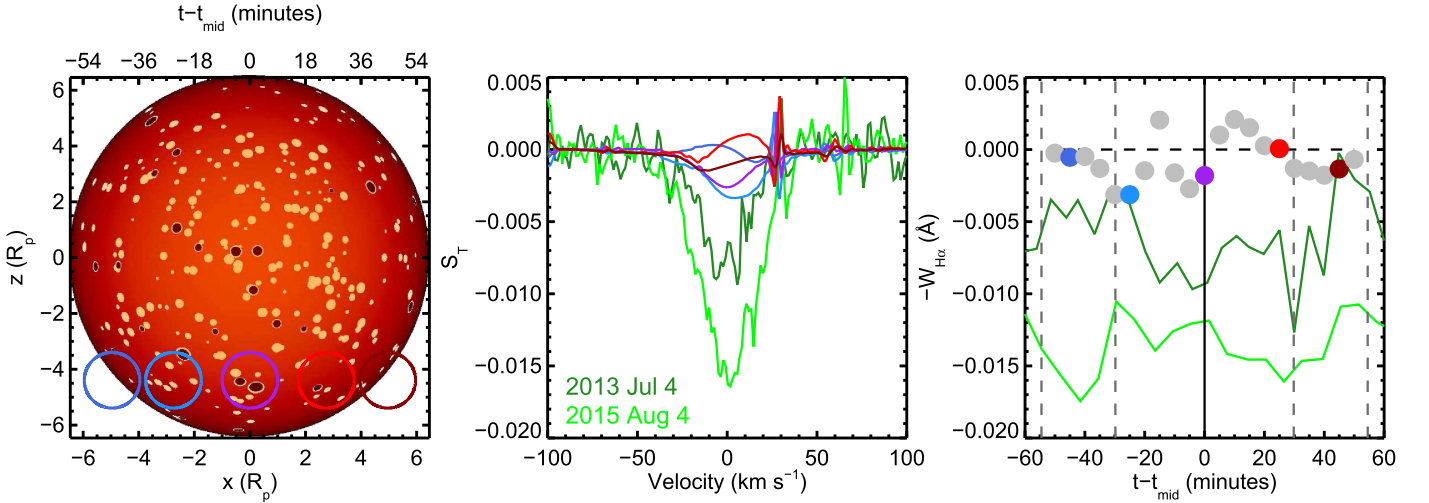


Figure 11. Same as Figure 9 but now with $A_{\text{sp}} = 0.01$, $Q = 0.13$, $A_{\text{fil}} = 0.0$, and $q_{\text{fac}} = 4.0$ for a uniform distribution of spots and facular regions. $W_{\text{H}\alpha}$ (right panel) is erratic since the planet never occults a large area of active regions. Note that q_{fac} is very large in this example but very similar behavior is seen for smaller values, although the variations in $W_{\text{H}\alpha}$ are smaller.

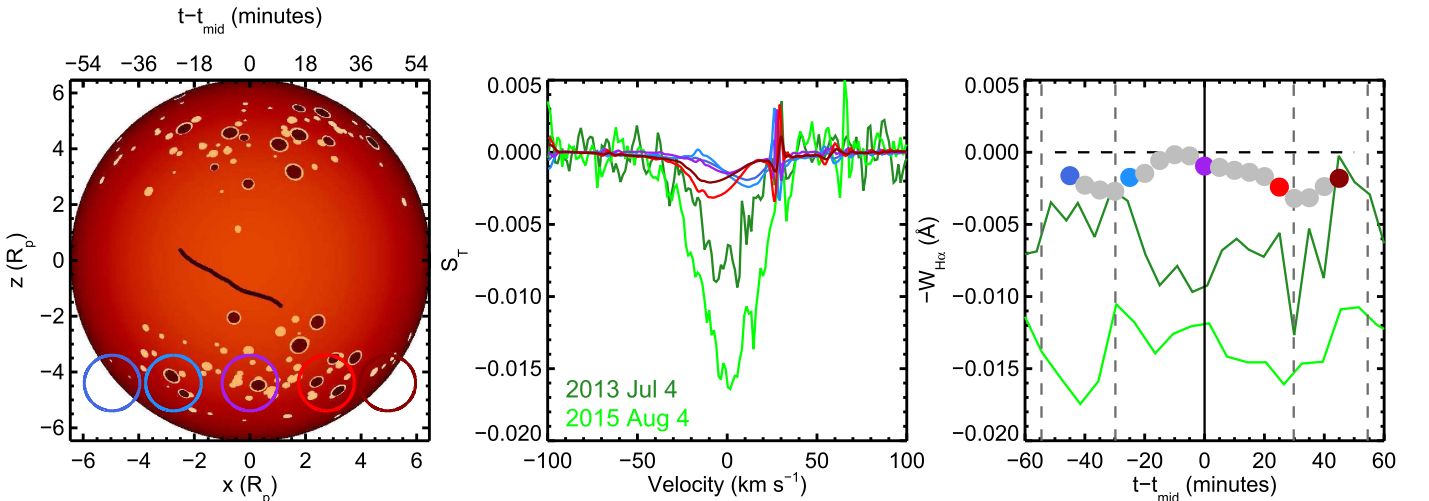


Figure 12. Same as Figure 9 but now with $A_{\text{sp}} = 0.02$, $Q = 0.5$, $A_{\text{fil}} = 0.005$, $\theta_{\text{act}} = \pm 40^\circ$, and $q_{\text{fac}} = 0.5$. Now the in-transit spectrum is weighted toward the photosphere since the planet occults active regions almost continuously throughout the transit. The contrast is strongest when the highest active region area is occulted, e.g., during the purple and red planet positions in the first panel. The $W_{\text{H}\alpha}$ values show absorption, although there is an abrupt shift near mid-transit when the planet begins to occult more of the facular regions.

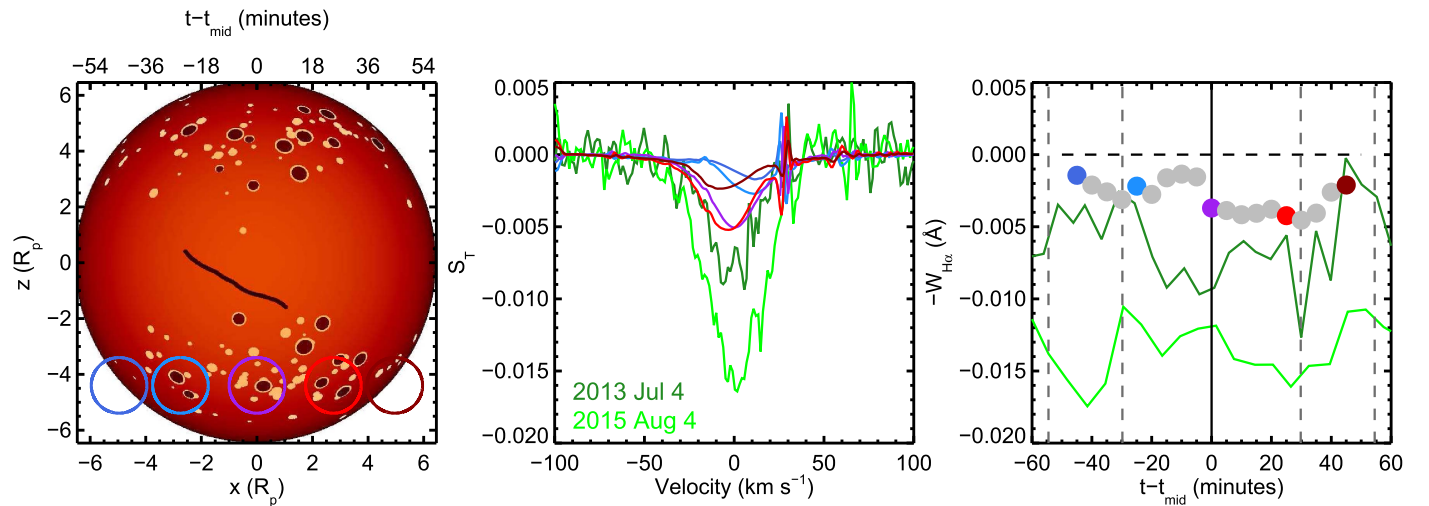


Figure 13. Same as Figure 12 but now with $q_{\text{fac}} = 1.5$. The stellar surface in the first panel is identical to that in Figure 12. The $W_{\text{H}\alpha}$ values show continuous absorption, although there is an abrupt shift near mid-transit when the planet begins to occult more of the facular regions. Although the contrast spectrum shows absorption throughout the transit, $W_{\text{H}\alpha}$ is still 2–3 \times smaller than is measured in most of the full transits from Figure 1.

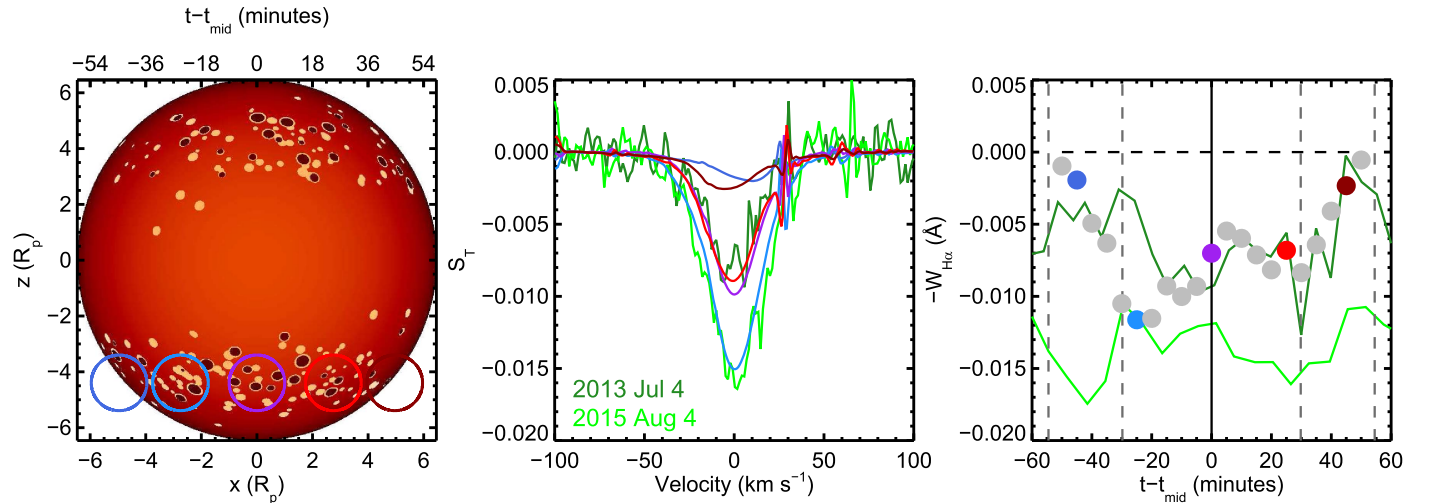


Figure 14. Same as Figure 8 but now with $A_{\text{sp}} = 0.03$, $Q = 0.15$, $A_{\text{fil}} = 0.0$, $\theta_{\text{act}} = 40^\circ$, and $q_{\text{fac}} = 4.0$. In this case facular/plage regions cover 20% of the stellar disk. The $W_{\text{H}\alpha}$ values show continuous absorption that is of comparable strength to the full $W_{\text{H}\alpha}$ transits seen in Figure 1.

were computed at fourteen values of $\mu = \cos(\theta)$ between 0.01 and 1.0. To avoid interpolation during the contrast model calculations, we fit the following limb-darkening law from Hestroffer & Magnan (1998) to each wavelength across the spectrum:

$$I(\mu) = 1 - u(1 - \mu^\alpha). \quad (5)$$

The parameters from Equation (5) are then used to compute $I(\mu)$ as a function of wavelength across the line for a densely sampled grid of μ across the stellar disk. Examples of the $I(\mu)/I(\mu = 1)$ versus μ curves and the corresponding Equation (5) fits are shown in Figure 7. There is a significant difference between the limb-darkening in the core of the line versus the line wing which can impact the measured $W_{\text{H}\alpha}$ values.

Figure 8 shows a transit example for a pure photosphere, i.e., no spots, faculae, or filaments. The only mechanism affecting the transmission spectrum or, in the absence of a planetary atmosphere, the contrast spectrum, is the CLVs described above. Five representative in-transit times are shown in the left

panel of Figure 8 and their corresponding S_T profiles are shown in the middle panel. The deepest contrast profiles are seen when the planet is near the stellar limb, but still almost completely covers the disk, since this is where the limb-darkening curves in the line wing and line core differ the most. The $W_{\text{H}\alpha}$ values for the entire in-transit calculation are shown in the right panel of Figure 8 which explicitly shows the “absorption” effect near the stellar limb.

An important take-away from the example shown in Figure 8 is that the signal induced by CLVs at $\text{H}\alpha$ is well below the measured $W_{\text{H}\alpha}$ values for most of the transit presented here. This is especially true for values of $W_{\text{H}\alpha}$ near mid-transit where the CLV effect is weakest. Although HD 189733 is an active star and thus it is unlikely that the visible hemisphere is ever pure photosphere, this baseline demonstrates that the observed $\text{H}\alpha$ transit signals cannot be caused by only CLVs in this specific case. However, the magnitude of the CLV effect is significant upon ingress and egress and must be included in any model of the in-transit absorption. It is also important to highlight the velocities of the S_T profiles in the middle panel of Figure 8: upon ingress, S_T shows redshifted velocities near

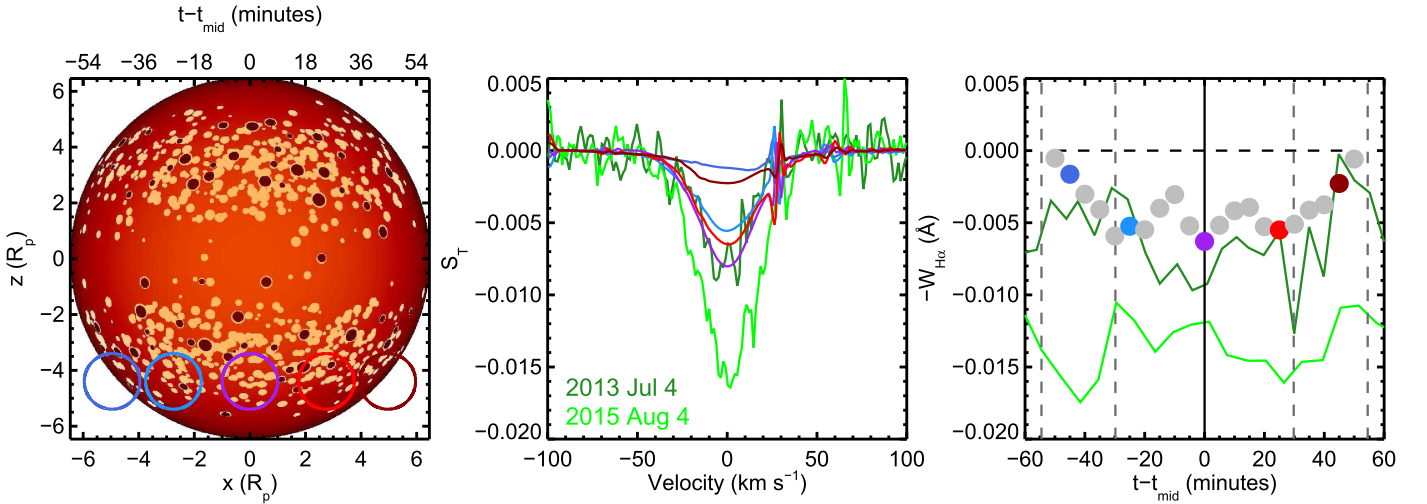


Figure 15. Same as Figure 14 but with $\theta_{\text{act}} = 30^\circ$, and $q_{\text{fac}} = 4.0$. The $W_{\text{H}\alpha}$ values are much weaker since the planet now transits the edge of the active region latitudinal belt. The $W_{\text{H}\alpha}$ values in the right panel are shown on the same scale as Figure 14 to emphasize the much weaker contrast effect.

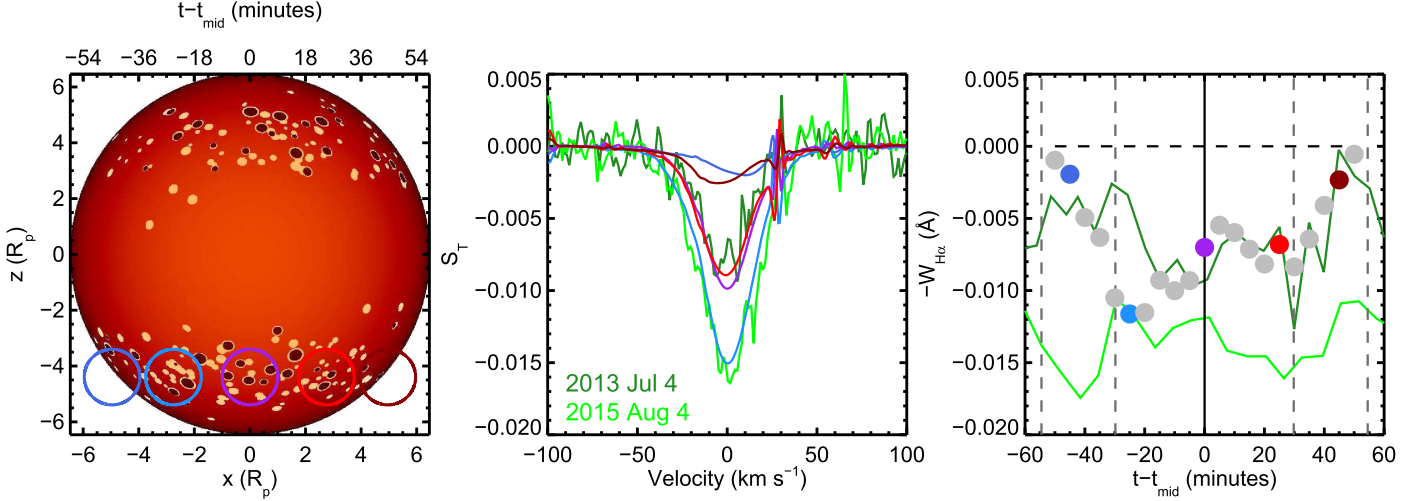


Figure 16. The less active case of $A_{\text{sp}} = 0.02$, $Q = 0.4$, $A_{\text{fil}} = 0.0$, and $q_{\text{fac}} = 4.0$. Although the facular/plage coverage is much lower than in Figure 14 $W_{\text{H}\alpha}$ is consistently observed in absorption across the whole transit.

maximum absorption while upon egress it shows blueshifted velocities. This contrast signal will have an important effect on the $v_{\text{H}\alpha}$ models presented in Section 7.

6.4. A Note on Parameter Importance

Specifying unique spectra and a unique spatial configuration for active regions on the stellar disk requires all of the parameters in Table 4. However, some of these parameters are much more important than others in determining changes in the contrast spectra. In addition, we can look to the observed $\text{H}\alpha$ transmission spectra and previous HD 189733 studies for guidance on other parameter values. For example, the spot radii actually govern the distribution of spots since larger spot radii means fewer spots for a constant A_{sp} . But A_{sp} is more important for determining the relative weights between spotted spectra and the photosphere, which in turn is more important for the contrast spectrum. The distribution of active regions is a strong determinant of the time series but does not strongly affect the contrast spectrum if the planet is not occulting a large fraction of the active regions. Another example is σ_{fac} of the active region emission. With the

assumption of the spectra being produced by the contrast effect, we can infer that $\sigma_{\text{fac}} \approx 40 \text{ km s}^{-1}$. This suggests that we do not need to explore a large range of values for σ_{fac} since most values will not be able to reproduce the line profile shape. For these reasons, although we have investigated the full range of parameters given in Table 4, we do not present details of the full extent of these efforts and instead focus on illuminating cases that are most relevant to the measurements.

6.5. Active Stellar Surface Transits

In this section we present various illustrative examples of the contrast effect for an active stellar surface. These examples are not meant to be exhaustive but rather representative of how general configurations affect the contrast spectrum and which parameters are most important in producing a significant contrast spectrum. We do not explore scenarios where the active regions are isolated to a small portion of the stellar disk since transits of these isolated regions have short durations. Instead, we explore scenarios that might produce absorption across the entire transit.

Table 5
Less-active Comparison Stars

ID (1)	T_{eff} (K) (2)	M_* (M_{\odot}) (3)	R_* (R_{\odot}) (4)	S_{HK} (5)
HD 189733	5040	0.81	0.76	0.51
HD 192263	4975	0.83	0.75	0.47
HD 104067	4956	0.91	0.75	0.34
HD 87883	4958	0.78	0.77	0.28

Note. HD 189733 parameters taken from Torres et al. (2008). All template stellar parameters are taken from Valenti & Fischer (2005). Values of S_{HK} are taken from Isaacson & Fischer (2010).

6.5.1. Transiting a Photospheric Chord

The planet can either transit active regions or the photosphere. Either way, the in-transit spectrum will be altered relative to the out-of-transit spectrum. Figure 9 shows an example of the planet transiting a chord with no active regions for the parameter values $A_{\text{sp}} = 0.02$, $Q = 0.7$, $A_{\text{fil}} = 0.0$, $\theta_{\text{act}} = 10^\circ$, and $q_{\text{fac}} = 1.5$. The CLVs can still be seen in the contrast profiles (middle panel) but since the in-transit spectra are weighted toward active regions, S_T shows emission in the line core at most $t-t_{\text{mid}}$ rather than absorption. This also shifts the $-W_{\text{H}\alpha}$ curve up toward less absorption.

One important thing to reiterate in this example is that strong absorption lines are not produced in the contrast spectra. This occurs for two reasons: (1) the facular core emission dominates the contrast spectrum; (2) the spot spectrum actually has a smaller core-to-continuum contrast compared with the photospheric spectrum. This reflects the fact that the $\text{H}\alpha$ line strength *decreases* for cooler stellar spectra. In this example, $\Delta T_{\text{sp}} = 700$ K so the spot spectrum is identical to that in Figure 6. This has important consequences for the pure-spot scenario, which we do not show: even without the core emission from the facular/plage regions, the contrast spectrum would still show core emission instead of absorption since the spot spectrum shows less core absorption than the photosphere. As a result, spots have little effect on the $\text{H}\alpha$ transmission spectrum.

We also show the filament-only case in Figure 10 for $A_{\text{fil}} = 0.01$. Filaments do not produce strong contrast spectra for reasonable values of A_{fil} , although we note that the average transmission spectrum (not shown) for an entire transit is seen in weak absorption for the case of the photospheric chord transit. Individual transmission spectra are seen in emission for transits of filaments. Since their contribution to the contrast effect is minor, even when the planet transits filaments, we do not focus on them further.

6.5.2. Transiting an Active Latitude

The photospheric transit examples demonstrate that $W_{\text{H}\alpha}$ cannot be measured in absorption if the planet does not consistently occult facular regions. Thus in order to produce the strongest $W_{\text{H}\alpha}$ curves shown in Figure 1 HD 189733 b must be transiting a chord that is densely covered with faculae and plage regions. Furthermore, as we demonstrate below, the emission strength in these facular regions must be similar to what is seen in flaring regions on the Sun.

Here we present examples of the planet transiting chords that contain active regions. The first scenario is shown in Figure 11 for uniformly distributed active regions with $A_{\text{sp}} = 0.01$, $Q = 0.13$,

$A_{\text{fil}} = 0.0$, and $q_{\text{fac}} = 4.0$. The $W_{\text{H}\alpha}$ time-series in the right panel is erratic; there is no trend. We have chosen the large value of $q_{\text{fac}} = 4.0$ to demonstrate that even very strong core emission cannot produce strong contrast spectra (center panel) if the planet never occults significant areas of active regions.

Figures 12 and 13 show examples of the planet transiting an active latitude. The active region configuration is identical in both cases. The only difference is in the value of q_{fac} : in Figure 12 $q_{\text{fac}} = 0.5$, while in Figure 13 $q_{\text{fac}} = 1.5$. The mid-transit times where the planet occults the largest area of facular regions show significant differences in the strength of the transmission spectrum: for the larger q_{fac} the absorption line is $\sim 2\times$ stronger. Furthermore, the $W_{\text{H}\alpha}$ values consistently show absorption across the entire transit whereas in the $q_{\text{fac}} = 0.5$ case $W_{\text{H}\alpha}$ approaches zero near mid-transit. These examples illustrate the important point that the strength of q_{fac} is the dominant factor in determining the magnitude of the contrast effect for any given transit snapshot. For the $W_{\text{H}\alpha}$ time-series, Q , and therefore the facular coverage fraction, is also important. But q_{fac} is the main determinant of the depth of the contrast spectrum. In neither case does the contrast effect produce absorption similar to what is observed.

The previous two examples demonstrate the need for greater contrast at $\text{H}\alpha$ in order to reproduce the observations. Figures 14 and 15 show scenarios with very high surface coverage fractions ($A_{\text{sp}} = 0.03$ and $Q = 0.15$ in both cases) and very strong facular/plage emission ($q_{\text{fac}} = 4.0$). The only difference is that the active region distribution in Figure 14 is centered at $\theta_{\text{act}} = \pm 40^\circ$ while in Figure 15 it is centered at $\theta_{\text{act}} = \pm 30^\circ$. In Figure 14 the planet transits an almost constant area of active regions and the strength of the facular emission produces strong contrast absorption lines (center panel) and a relatively uniform $W_{\text{H}\alpha}$ timeseries (right panel). Although q_{fac} is the same in Figure 15 the contrast profiles are weaker and $W_{\text{H}\alpha}$ is $\sim 3\times$ shallower. This is the result of the planet transiting the edge of the active region distribution where, at any in-transit snapshot, the planet occults a relatively smaller area of facular/plage regions compared to the distribution in Figure 14. This suggests that the active regions on HD 189733's surface must be centered very near the planet's transit chord in order to produce a relatively uniform $W_{\text{H}\alpha}$ time-series.

The value of Q in the above examples, which equates to a 20% surface coverage of facular/plage regions, does not necessarily need to be so low, i.e., the active region surface coverage does not need to be so large. Figure 16 shows the case for $A_{\text{sp}} = 0.02$, $Q = 0.4$, $A_{\text{fil}} = 0.0$, and $q_{\text{fac}} = 4.0$. While $W_{\text{H}\alpha}$ is not as uniform, the values during the first half of the transit approach the largest observed values from Figure 1. We note that moving the center of the active region distribution to $\pm 30^\circ$ latitude results in essentially no contrast for the entire transit. This again illustrates the need for the active regions to be concentrated near the transit chord and to be uniformly distributed in longitude. It also shows that if Q increases, q_{fac} must remain high or even increase in order to get close to the observed values; decreasing q_{fac} from 4.0 to ~ 2.0 produces a very weak contrast effect.

6.6. Comparisons with Low-activity Templates

We demonstrated above that it is possible under some conditions to reproduce even the strongest observed $W_{\text{H}\alpha}$ in-transit signals using the contrast effect. However, the only parameter configurations that are able to produce these $W_{\text{H}\alpha}$

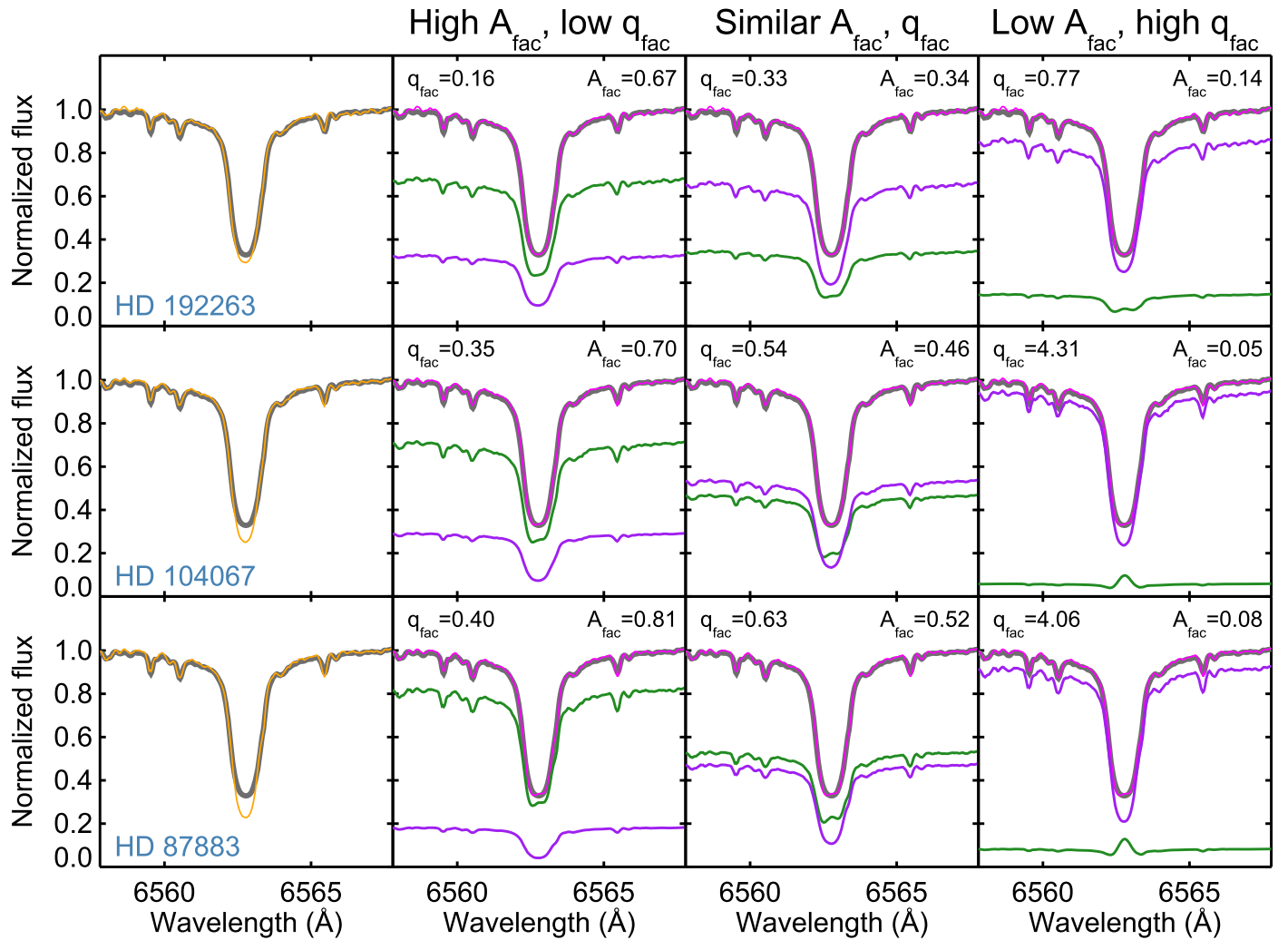


Figure 17. Comparison of HD 189733 $H\alpha$ profile with less active main sequence templates. Column 1 shows the observed template overplotted in orange on top of the HD 189733 spectrum (dark gray line). Columns 2–4 show various combinations of A_{fac} and q_{fac} from Equation (6) that are needed to reproduce the HD 189733 $H\alpha$ core depth. The photospheric spectrum is shown in purple and the facular/plage spectrum is shown in green. A clear relationship is seen for A_{fac} and q_{fac} : as q_{fac} increases, A_{fac} must decrease to produce the same disk-integrated spectrum. This implies that we cannot use both high A_{fac} and high q_{fac} to describe the observed $H\alpha$ transits since it would violate the observed disk-integrated core strength.

values involve modest to large facular coverage fractions and $q_{\text{fac}} \sim 4\text{--}5$. Although we do not know exactly how the active regions are distributed on HD 189733 or the strength of the facular/plage $H\alpha$ core emission, we can attempt to roughly constrain the *combination* of these parameters by comparing HD 189733 with less active main sequence templates of similar T_{eff} .

We have downloaded archived Keck HIRES data for the three template stars listed in Table 5. HD 189733 is also listed for comparison. We use these templates to find parameter combinations of q_{fac} and A_{fac} , where A_{fac} is the fractional surface area covered by facular regions, that can fill in the $H\alpha$ absorption of the less-active template and match the line profile of HD 189733. Note that A_{fac} is just another way of specifying Q in the contrast models, where $Q = A_{\text{sp}}/A_{\text{fac}}$. The HD 189733 spectrum is an average of the comparison spectra used in all of the Keck transits (purple circles in Figure 1). The facular spectrum S_{fac} is constructed in the same manner as the contrast model facular spectrum except now q_{fac} refers to the core flux of the template spectrum. The final spectrum is the weighted average of the photospheric spectrum S_{phot} , which is the

observed template spectrum, and S_{fac} :

$$S_{\text{tot}} = (1 - A_{\text{fac}})S_{\text{phot}} + A_{\text{fac}}S_{\text{fac}}. \quad (6)$$

While all of the observed template spectra are rotationally broadened according to the $v \sin i$ value of HD 189733, we do not account for the CLVs discussed previously. Thus we are only exploring first-order approximations for which q_{fac} and A_{fac} values are needed to reproduce the HD 189733 $H\alpha$ core. Since we do not have spatially resolved spectra of these stars we cannot build up the spectrum across the stellar disk as is done in the contrast model case.

Three different parameter combinations are shown for each template in Figure 17. A χ^2 minimization routine is used to produce the fits for various initial parameter combinations that correspond roughly to the parameter space explored in each column. The first column shows a direct comparison between HD 189733 (dark gray line) and the templates (orange lines). Column 2 shows the case of high A_{fac} and low q_{fac} , i.e., weak facular emission but distributed across much of the stellar disk. Column 3 shows slightly stronger q_{fac} but reduced A_{fac} . Finally, column 4 shows large q_{fac} and small A_{fac} . We note that the HD

189733 spectrum is also plotted in columns 2–4 but is obscured by the model fits.

For all three templates, a crucial trend is seen: as q_{fac} increases, A_{fac} must decrease for a given photospheric spectrum. This is not surprising but has important consequences for which parameter combinations in the contrast model are likely to be representative of HD 189733's active surface. For example, the very low Q and very high q_{fac} case shown in Figure 14 is unlikely to accurately represent the stellar surface since the same parameter combination would drastically overestimate the line core emission in Figure 17. However, the less active case in Figure 16 seems plausible: similar values of q_{fac} and Q , or a facular coverage fraction of $\sim 8\%$, are seen in the low A_{fac} , high q_{fac} case for HD 87883 in Figure 17.

One important caveat to the template comparison is that the template spectra themselves contain some contribution from active regions. Thus we are not comparing pure photospheres to HD 189733's active surface. However, this does not affect the relationship between q_{fac} and A_{fac} ; one must decrease as the other increases for a specific template spectrum, pure photosphere or not. On the other hand, the *value* of the parameters in Figure 17 may be affected. For example, instead of $A_{\text{fac}} = 0.08$ and $q_{\text{fac}} = 4.06$ in the lower right panel of Figure 17, one or both values would need to be larger if HD 87883's spectrum contained no contributions from active regions. Thus the parameter combinations shown in Figure 17 are likely lower limits to the true values.

6.7. Discussion and Summary of Contrast Results

We have presented transit models for a planet with no atmosphere in order to explore the contrast effect in $H\alpha$ that is produced when in-transit spectra, for which a portion of the stellar disk is occulted, are compared with out-of-transit spectra. We find the following.

1. Spots and filaments, for the physically reasonable surface coverage fractions and spot/filament parameters explored here, are unimportant in the $H\alpha$ contrast spectrum. The main contribution to the contrast effect comes from strong facular or plage emission.
2. Transits of the photosphere do not produce $H\alpha$ contrast in absorption; active regions that include strong faculae/plage emission must be transited to produce S_T in absorption.
3. The facular coverage fraction must be $\gtrsim 5\%$ – 10% and these facular regions must be concentrated around the transit chord in order for the strongest observed $H\alpha$ transits to be reproduced. Large coverage fractions, no matter the value of q_{fac} , cannot reproduce the observed $H\alpha$ line profiles if the distribution is uniform across the stellar disk. This holds true even for very large coverage fractions of $>50\%$ since the contrast spectrum then begins to be weighted back toward the active region spectra, producing emission instead of absorption.
4. Certain configurations of facular regions combined with values of $q_{\text{fac}} \sim 4.0$ are able to produce relatively uniform transits with depths of $W_{H\alpha} \approx 0.007$ – 0.015 , similar to the observed transits shown in Figure 1.
5. The comparison of less active template stars to HD 189733 suggests that for $q_{\text{fac}} \sim 4$ the facular coverage fraction must be $\gtrsim 5\%$ – 10% . This is similar to what is

needed to reproduce the observed transits, although these are lower limits since the templates do not represent pure stellar photospheres.

While our simulations show that the contrast effect is able to reproduce the observed in-transit $W_{H\alpha}$ values, it is unclear whether the necessary parameters are physically realistic. We believe facular coverage fractions of $\sim 10\%$, and possibly higher, are not unreasonable considering the stronger activity level of HD 189733 compared with the Sun. Solar facular coverage can reach $\sim 5\%$ during solar active periods (Shapiro et al. 2015) and plage coverage can reach $\sim 8\%$ (Foukal 1998). On the other hand, Shapiro et al. (2015) (see also Foukal 1998; Lockwood et al. 2007) find that photometric variations for more active stars are spot-dominated and that the ratio of facular/plage coverage to spot coverage *decreases* with increasing activity level. Lanza et al. (2011) find that RV modulations in HD 189733's spectrum are best modeled with values of $Q = A_{\text{fac}}/A_{\text{spot}} \sim 0$, i.e., they find no evidence of facular/plage effects on the measured RV values. Furthermore, Lanza et al. (2011) find spot filling factors of $\sim 1\%$ are able to reproduce HD 189733's photometric variations across roughly four weeks of nightly observations. Similar spot coverages are found by Herrero et al. (2016) for the same data set. This would suggest values of $Q = 0.1$ for the contrast model in order to produce $\sim 8\%$ facular/plage coverage.

The larger question for $H\alpha$ contrast models is what constitutes a reasonable value of q_{fac} . We have shown that $q_{\text{fac}} \gtrsim 4.0$ is needed in order to produce values of $W_{H\alpha}$ similar to what is observed. If this is the case, then the normal or quiescent facular/plage regions on HD 189733 have $H\alpha$ emission line strengths similar to moderate flaring regions on the Sun. Magnetic fields play an important role in heating the chromosphere and producing bright regions in the atmosphere (e.g., Hansteen et al. 2007). Indeed, simulations of $H\alpha$ brightness in solar active regions show that the brightest regions correspond to the strongest local magnetic field strengths (Leenaarts et al. 2012). HD 189733 has a much stronger global magnetic field than the Sun, with radial field values reaching 30–40 G across much of the stellar surface (Fares et al. 2010). Thus the larger field values, and consequently heating rates, could have a significant effect on the emission strength of $H\alpha$ in active regions.

A final consideration is the requirement that the facular/plage regions be concentrated very close to the planetary transit chord, or a latitude very near $+40^\circ$. Active latitudes are known features of the solar surface (e.g., Vecchio et al. 2012) and have been inferred via photometric transits for other stars as well (Sanchis-Ojeda & Winn 2011; Kirk et al. 2016). Lanza et al. (2011) find that spots near $\approx 30^\circ$ – 40° are able to best reproduce the measured RV variations. Thus it is not unreasonable that the facular/plage regions are located near the transit chord. The specificity required, however, to reproduce any of the observed $W_{H\alpha}$ transits is a concern, especially if active latitudes migrate as a function of time.

Although we cannot conclusively distinguish between models in which the observed $W_{H\alpha}$ transits are due to absorption by the planet or from the contrast effect, we believe the parameter values required to reproduce the observations are specific and likely do not represent the average stellar disk of HD 189733. Furthermore, the contrast effect cannot explain the $W_{H\alpha}$ values seen in absorption immediately before the 2013 July 4 transit, before and after the 2015 August 4 transit, and immediately after

the 2006 August 21 transit, i.e., these extended transits are suggestive of absorbing circumplanetary material. In addition, we demonstrated in Cauley et al. (2017) that these pre- and post-transit signatures are abnormal and must be related to the planetary transit, further making the case for a circumplanetary origin. More detailed modeling of $H\alpha$ spectral line profiles in faculae and plages for active stars are needed to determine if the large core strengths used here are realistic. For now, however, we favor the planetary interpretation.

7. $H\alpha$ Velocity Measurements and Models of Planetary Rotation

Barnes et al. (2016) presented an analysis of the same three HARPS transits presented in this work. They noted a trend in the velocity centroids of the $H\alpha$ transmission spectra, when calculated in the frame of the planet, moving from redshifted to blueshifted (their Figure 3). This is cited as evidence that the absorption may not arise in the planetary atmosphere since the absorption line profiles should be centered at zero velocity in the planetary reference frame. In this section we present measurements of the $H\alpha$ transmission spectrum velocity centroids and models of atmospheric absorption which include planetary rotation. We demonstrate that velocities in the upper atmosphere of HD 189733 b might explain the in-transit velocity trends identified by Barnes et al. (2016).

To date, only a handful of studies have presented observational signatures of atmospheric dynamics for massive exoplanets. The first detection of a day-to-night side wind, a result consistent with predictions by a variety of detailed hot Jupiter circulation models (e.g., Showman & Guillot 2002; Showman et al. 2009; Menou & Rauscher 2010; Rauscher & Menou 2010; Rauscher & Kempton 2014), was made by Snellen et al. (2010) for HD 209458 b. They observed a $\sim 2 \text{ km s}^{-1}$ blueshifted offset in a CO absorption signal which matches closely with the magnitude of the flow velocity from atmospheric models (e.g., Showman et al. 2008). Snellen et al. (2014) measured an equatorial rotational velocity of 25 km s^{-1} for the young massive planet β Pic b using cross-correlated thermal signatures of CO and H_2O . Wyttenbach et al. (2015) measured an $8 \pm 2 \text{ km s}^{-1}$ blueshift in the NaI doublet and suggested that the large velocity might be the result of high-altitude winds.

Most recently, studies by Louden & Wheatley (2015) and Brogi et al. (2016) have demonstrated detections of the planetary rotational velocity and day-to-night side winds of HD 189733 b. For NaI, Louden & Wheatley (2015) also claim a detection of a spatially resolved, eastward super-rotating equatorial jet. Brogi et al. (2016) search for a similar feature in their near-IR CO measurement but are unable to place constraints on a jet velocity. Both studies find planetary rotational velocities that are consistent with synchronous rotation and day-to-night side wind speeds of $\sim 2 \text{ km s}^{-1}$. The results of Brogi et al. (2016) and Louden & Wheatley (2015) demonstrate the exciting possibility of measuring the atmospheric dynamics of hot Jupiter atmospheres using ground-based, high-resolution spectra.

In Cauley et al. (2016) we presented an $H\alpha$ velocity measurement (see Equation (7) below) and the corresponding in-transit $v_{H\alpha}$ values for two Keck HIRES transits. Barnes et al. (2016) investigated the $H\alpha$ line velocities of the three HARPS data sets examined in this paper. They present velocity profiles as a function of orbital phase (see Figure 3 of Barnes et al. 2016) but do not calculate velocities for individual absorption line profiles. They reference visual features in the

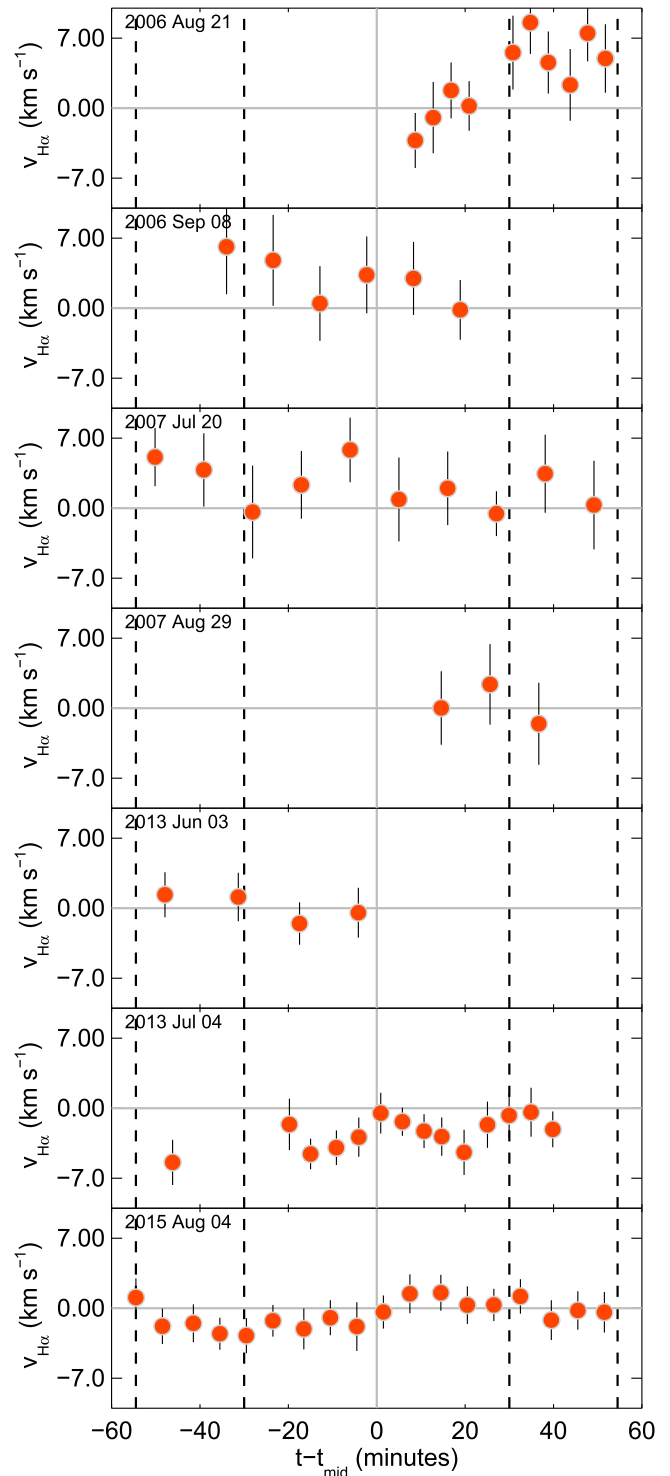


Figure 18. Values of $v_{H\alpha}$ from Equation (7) for all in-transit points showing 1σ absorption. The uncertainties for most of the HARPS measurements are $\sim 3\text{--}4 \text{ km s}^{-1}$ while the Keck uncertainties are $\sim 1\text{--}2 \text{ km s}^{-1}$. The vertical dashed lines mark the transit contact point. There are no clear patterns in the velocity measurements for any of the transits except 2015 August 4.

velocity maps as evidence of trends in the line velocities across the transit. Here we present explicit velocity measurements of the individual HARPS and Keck spectra. As we show below, the individual HARPS transmission spectra are fairly noisy and result in highly uncertain values of $v_{H\alpha}$. The Keck velocities are more tightly constrained due to the much higher S/N of the $H\alpha$ spectra.

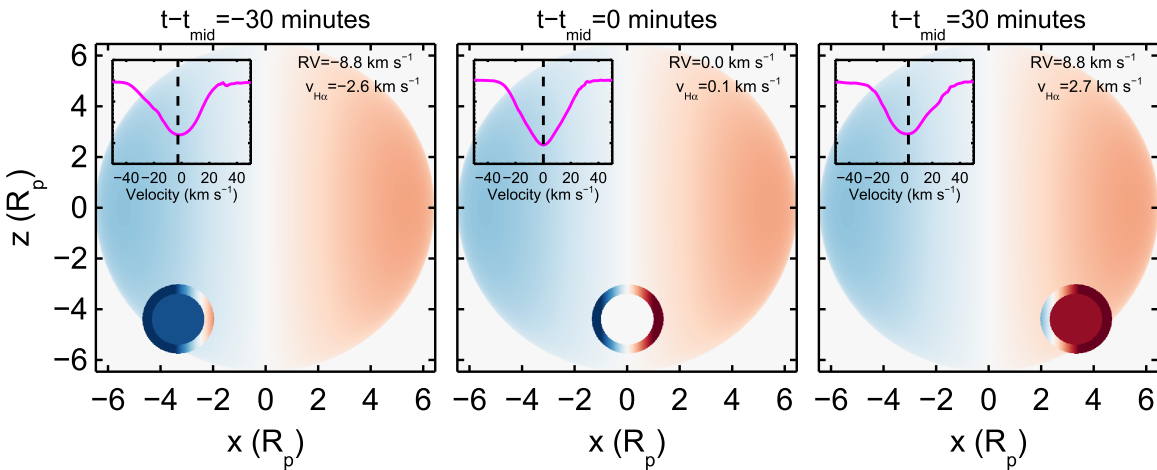


Figure 19. Example of how planetary rotation affects the measured transmission spectrum. The colors are representative of the radial velocity of the colored portion. Darker colors represent larger velocities. The stellar rotational velocities are weighted by the limb-darkened intensity to visually represent the weighted velocity contribution of the stellar disk. The bulk motion of the planetary disk is given a single color and is given in the upper-right of each panel. The measured $v_{\text{H}\alpha}$ from Equation (7) for the in-laid magenta transmission spectrum is also given in the upper-right corner. The $v_{\text{H}\alpha}$ values are much lower than the planetary RV for times when the planet is near the limb, suggesting that any planetary rotation will reduce the measured line velocities. This example shows absorption lines for an atmosphere with $T_{\text{exo}} = 7800$, $v_{\text{rot}} = 10 \text{ km s}^{-1}$, $b = 4.0 \text{ km s}^{-1}$, and $\rho = 3.0 \times 10^{-23} \text{ g cm}^{-3}$. Note that the individual $v_{\text{H}\alpha}$ values do not change much for different values of T_{exo} , b , and ρ ; they are dominated by v_{rot} .

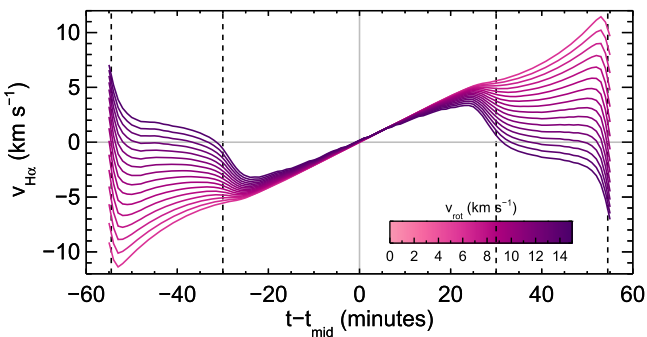


Figure 20. $\text{H}\alpha$ transmission spectrum velocity measurements, defined by Equation (7), as a function of time from mid-transit. The color indicates the equatorial planetary rotational velocity, the values of which are specified in the inset color bar. The transit contact points are marked with vertical dashed lines. As the planet rotates faster, absorption lines in the planetary atmosphere are shifted further away from the planetary orbital velocity upon ingress and egress, creating the slope changes in $v_{\text{H}\alpha}$ seen near ± 25 minutes. Even the case of no rotation shows a depressed line velocity compared with the orbital velocity. This is due to the CLVs described in Section 6. This set of models was calculated with the same atmospheric parameters used in Figure 19.

We perform all of our velocity analysis in the stellar rest frame. After correcting the observed spectra for the system radial velocity and the Earth’s heliocentric motion, this is also the frame of the observer. Shifting the transmission spectra by the planetary radial velocity can confuse and mask atmospheric velocities that may be contributing to the line profile, as we demonstrate below.

The line velocity index from Cauley et al. (2016) is defined as:

$$v_{\text{H}\alpha} = \frac{\sum_{v=-40}^{+40} v(1 - F_v)^2}{\sum_{v=-40}^{+40} (1 - F_v)^2} \quad (7)$$

where F_v is the transmission spectrum flux at velocity v . The index is essentially the velocity vector v weighted by the square of the transmission spectrum flux. The square of the flux is

chosen to provide stronger weight to deeper portions of the transmission spectrum. We only calculate $v_{\text{H}\alpha}$ for observations that show $\geq 1\sigma$ absorption. The uncertainty on the individual $v_{\text{H}\alpha}$ points is calculated by taking the standard deviation of the mean of velocities corresponding to the $(1 - F_v)^2$ values that comprise 68% of the total weight. This produces larger uncertainties for lines where the weights are comparable at many different velocities, which is the case for the noisy HARPS S_T profiles. The measured $v_{\text{H}\alpha}$ values are shown in Figure 18. The typical HARPS uncertainties are $\sim 3\text{--}4 \text{ km s}^{-1}$ while the Keck uncertainties are $\sim 1\text{--}2 \text{ km s}^{-1}$, although they are slightly larger for the 2006 August 21 transit.

It is clear from Figure 18 that there is no obvious $v_{\text{H}\alpha}$ trend across epochs, even for the transits that show consistent $W_{\text{H}\alpha}$ values in absorption (e.g., 2007 July 20, 2013 July 4, and 2015 August 4). The only date that shows any transit pattern is 2015 August 4: the velocities change from slightly blueshifted to slightly redshifted from the first half of the transit to the second, although the mean of $v_{\text{H}\alpha}$ for each half of the transit is only different from zero at the $\sim 1\text{--}2\sigma$ level. The 2013 July 4 transit shows a mild blueshifted offset of $\sim 2 \text{ km s}^{-1}$ but $v_{\text{H}\alpha}$ values from the first half of the transit are plagued by weak $W_{\text{H}\alpha}$ values. Little information is gleaned from the partial transits. We will explore the 2015 August 4 trend using models of planetary rotation and velocities as a product of the contrast effect from Section 6.

7.1. Planetary Rotation Models

In order to explore physical scenarios for the $\text{H}\alpha$ line velocities presented above, we have simulated transmission spectra through a rotating planetary atmosphere. We use the same stellar and planetary parameters that were presented in Section 6 and the same PHOENIX model spectra are used as the intrinsic stellar spectra. We neglect active regions on the stellar surface and assume a pure photosphere (see Section 7.2). The stellar radial velocity as a function of in-transit time is included in the line profile calculations.

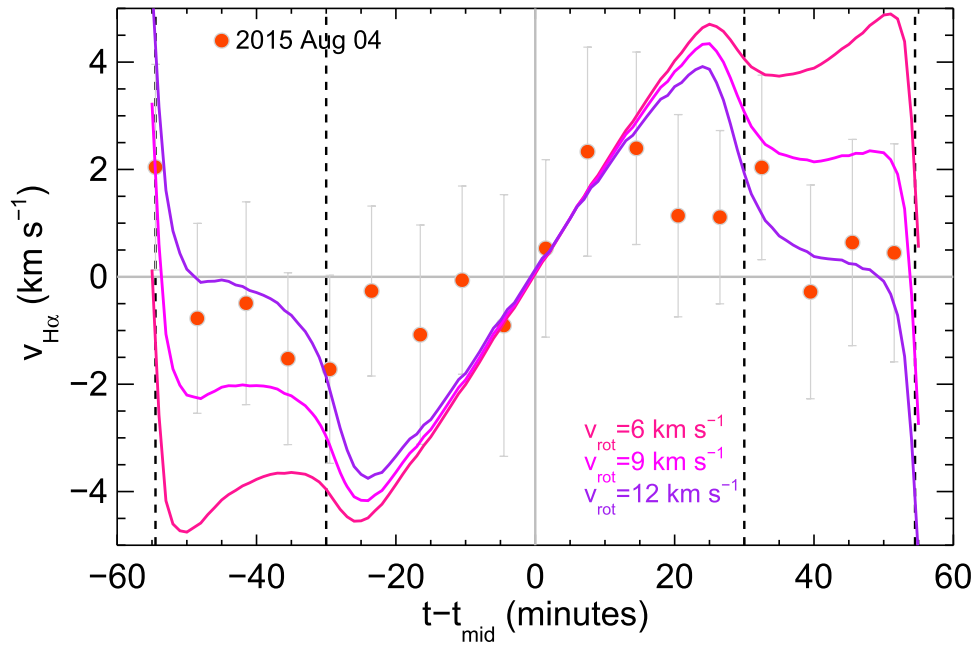


Figure 21. Comparison of planetary rotation models with the observed $v_{\text{H}\alpha}$ values from the 2015 August 4 transit. Three representative rotation models from Figure 20 are shown and the plot scale is reduced to show the detailed shape of the model curves. The models produce essentially identical $v_{\text{H}\alpha}$ values between second and third contact and do a poor job of matching the data for times immediately after second contact and immediately before third contact. However, the $v_{\text{rot}} = 9$ and 12 km s^{-1} models show similar $v_{\text{H}\alpha}$ values compared with the data between first and second and third and fourth contacts.

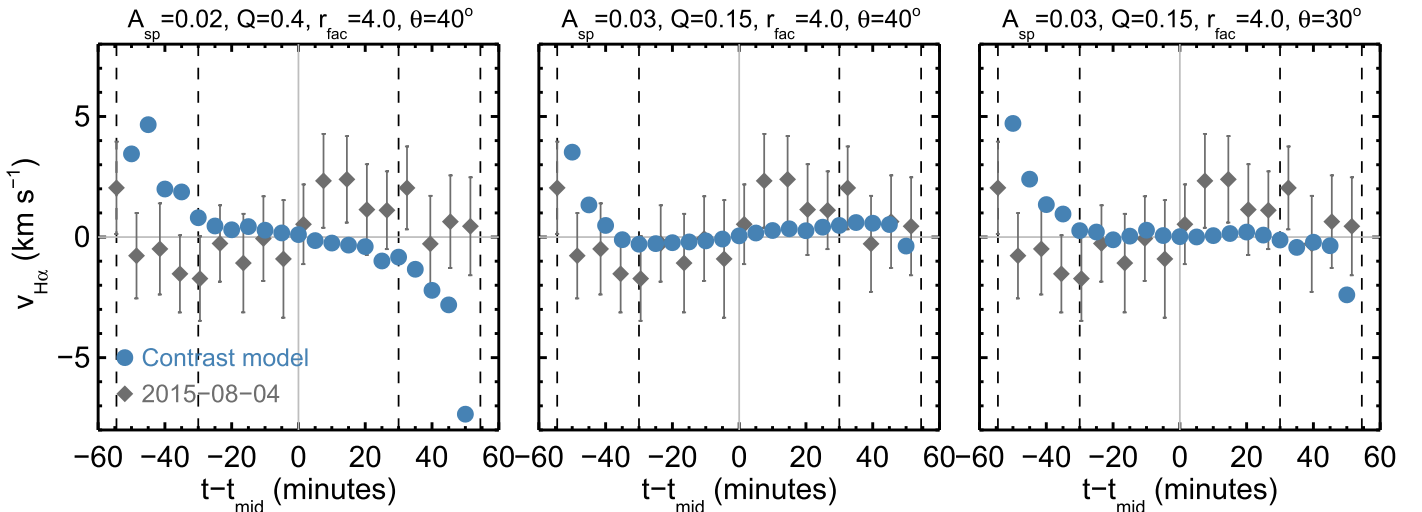


Figure 22. Velocities from the contrast models (blue circles) overplotted on the $v_{\text{H}\alpha}$ values from the 2015 August 4 transit. The left panel corresponds to the contrast model in Figure 16, the middle panel to Figure 14, and the right panel to Figure 15. The contrast velocities from the middle panel do a fair job of reproducing the observed $v_{\text{H}\alpha}$ values. Other contrast scenarios besides the very active case do not reproduce the observations well and in fact show the opposite trend, i.e., a transition from redshifted to blueshifted velocities from the first half to the second half of the transit.

The planetary atmosphere is assumed to be of uniform density. This choice is motivated by the models of Christie et al. (2013) who found that the number density of $n = 2$ hydrogen was approximately constant across 3–4 orders of magnitude in atmospheric pressure. Assuming a hydrostatic versus uniform density atmosphere has little effect on the simulations. The planetary $\text{H}\alpha$ absorption profile is approximated as a velocity-broadened delta function where the broadening parameter is labeled b (Draine 2011; Cauley et al. 2015, 2016). The planet is assumed to rotate rigidly throughout the atmosphere.

We have also investigated the effects of superrotating equatorial jets (Showman et al. 2008; Rauscher & Menou 2010) and find that they produce similar effects as rigid rotation, although the jet velocities required to produce the same line profiles are larger than the rotational velocities since the jets occupy a smaller portion of the atmosphere. We do not include jets explicitly in the rest of the model discussion but we will discuss them as part of the general effect of large rotational velocities.

Figure 19 shows the effect of a rotating atmosphere on the transmission spectrum for a prograde planetary orbit. Upon ingress

(left panel) the portion of the planet’s atmosphere dominating the transmission spectrum is moving *away* from the observer while the planet’s bulk motion is *toward* the observer. The net effect is to produce a measured centroid velocity, or in our case $v_{H\alpha}$, that is significantly less than the bulk planetary velocity. This was first demonstrated by Miller-Ricci Kempton & Rauscher (2012, their Figure 8) and reiterated in Loudén & Wheatley (2015, their Figure 2). The same effect is seen upon egress (right panel).

Simulated $v_{H\alpha}$ curves for the entire transit are shown in Figure 20 where the effect of higher rotational velocities can be seen in the suppression of $v_{H\alpha}$ relative to the line-of-sight orbital velocity upon ingress and egress. For the highest rotational velocities, the atmosphere is moving fast enough to cause $v_{H\alpha}$ to have the opposite sign compared to the planet’s bulk motion. We note that for strong atomic lines, even the case of no rotation, produces suppressed line velocities due to the CLVs discussed in Section 6. For transits that are sampled asymmetrically in time, CLVs could produce velocity shifts in the average transmission spectrum (e.g., see Loudén & Wheatley 2015; Wyttenbach et al. 2015).

Figure 20 shows that for sufficiently large v_{rot} the measured $v_{H\alpha}$ values can be very small or even have the opposite sign relative to the planetary bulk velocity. While these transit curves cannot explain the erratic velocities of the HARPS data or the 2006 August 21 Keck data, they may provide evidence for what we are seeing in the 2013 July 4 and 2015 August 4 Keck transits and perhaps the first half of the 2013 June 3 transit.

Figure 21 shows three different rotation models plotted against the 2015 August 4 $v_{H\alpha}$ values. Rotational velocities $\lesssim 9 \text{ km s}^{-1}$ do not match the data well; velocities between 10 and 12 km s^{-1} are required to produce the small $v_{H\alpha}$ values between first and second and third and fourth contact. Values of $v_{\text{rot}} \gtrsim 12 \text{ km s}^{-1}$ begin to produce $v_{H\alpha}$ values that are too small, i.e., of the wrong sign. The models do not do a good job of reproducing $v_{H\alpha}$ near -20 and $+20$ minutes; all of the models produce $v_{H\alpha}$ larger than the measured values. Overall, however, these models demonstrate that large velocities in the extended atmosphere can produce the small observed velocities.

7.2. Velocities from Contrast Models

It is possible for certain contrast model scenarios to produce $v_{H\alpha}$ values similar to what is observed for the 2013 July 4 and 2015 August 4 transits. We have calculated $v_{H\alpha}$ for the contrast model line profiles. The $v_{H\alpha}$ values for the contrast models from Figure 16 (left panel), Figure 14 (middle panel), and Figure 15 (right panel) are shown in Figure 22. The contrast model line profiles show trends similar to the 2015 August 4 data, although only the very active case (middle panel) shows the blueshifted to redshifted pattern from the first half of the transit to the second half. Although not shown here, all of the other cases explored in Section 6 show something similar to the left panel of Figure 22: large redshifted velocities during the first half of the transit and blueshifted velocities during the second half. More active cases than the middle panel tend to move in the other direction: larger and larger blueshifted velocities and then redshifted velocities during the second half.

Overall, the velocities from the contrast models do not reproduce the observed 2015 August 4 velocities except for the case of a very active stellar surface with the active regions centered very near the planet’s transit chord (see Figure 14). For this reason, and those given concerning the planetary rotation models, we do not believe the contrast velocities

represent a convincing explanation for the observations. However, further in-transit observations should be conducted to strengthen or reject this argument.

7.3. Discussion of the Rotation Models and $H\alpha$ Velocities

The rotation models presented here are meant to demonstrate that the low velocities, i.e., much less than the in-transit planetary line-of-sight velocity, observed in the $H\alpha$ transits are not necessarily intrinsic to the star because of their magnitude. While very hot Jupiters such as HD 189733 b are generally assumed to be synchronously rotating, there are no measurements of hot Jupiter rotation rates outside of the studies done by Brogi et al. (2016) and Loudén & Wheatley (2015), who both found evidence for a synchronously rotating HD 189733 b. However, these measurements were made in CO⁸ (Brogi et al. 2016) and NaI (Loudén & Wheatley 2015). The CO measurements probe much higher pressures deeper in the atmosphere than $H\alpha$ and NaI, which probe pressures of 10^{-6} – 10^{-9} bar (Christie et al. 2013; Wyttenbach et al. 2015). The NaI measurements by Loudén & Wheatley (2015) do not examine the velocities of individual observations and instead fit the average in-transit line profile. Loudén & Wheatley (2015) also do not include differential limb darkening, opting to use a broadband limb-darkening law. This could significantly affect the velocities of the model line profile (Czesla et al. 2015) and should be investigated.

Even if a hot Jupiter is synchronously rotating, velocities larger than the equatorial rotational velocity may be present in the extended atmosphere. Rauscher & Kempton (2014) find wind speeds of ~ 7 – 11 km s^{-1} in the upper atmospheres of both a synchronously and a quickly rotating HD 189733 b. Their models were calculated at pressures of 10^0 – 10^{-6} bar, which begins to probe the potential $H\alpha$ formation region. Thus it is not implausible that even stronger winds may form at higher altitudes or that unexplored atmospheric dynamics are contributing to the $H\alpha$ transmission spectra.

While the most active contrast model is able to produce $v_{H\alpha}$ values similar to what is observed for the 2015 August 4 transit, we do not believe this is the correct model due to required specificity of the model parameters. In other words, matching the velocities requires all of the most active contrast model parameters to be accurate whereas matching only the $W_{H\alpha}$ observations provides more leeway in the active region coverage fraction and facular emission line strength. On the other hand, the 2015 August 4 transit does seem to be unique in that it shows the largest $W_{H\alpha}$ signal and the strongest out-of-transit Ca II emission. Although it seems unlikely, we cannot definitively rule out the most active case as an explanation for the both $W_{H\alpha}$ and $v_{H\alpha}$.

We emphasize that the $H\alpha$ transits do not show a consistent velocity signal across epochs, and as a result no firm conclusions can be reached concerning their origin. The individual HARPS spectra are especially noisy and the velocity uncertainties derived here are large, making them even less useful for understanding the in-transit signal. Further short-cadence $H\alpha$ transit observations are needed to work toward clarifying the velocity signal and, by extension, the in-transit $H\alpha$ absorption line profiles.

⁸ Brogi et al. (2016) measure the strongest signal in CO but also marginally detect H₂O.

8. Summary and Conclusions

We have presented an analysis of $H\alpha$ transmission spectra for seven transits of HD 189733 b that span almost a decade. Five of these $H\alpha$ transits are from archival HARPS and Keck data, while two were previously analyzed by our group in Cauley et al. (2015, 2016). Four of these transits show significant and consistent $H\alpha$ spectra in absorption throughout the transit while three others show strong variations that may be due to changes in stellar activity. The irregular changes may also be due to transiting gas not bound to the planet. Our main conclusions are as follows.

1. We do not find evidence of a clear relationship between the stellar activity level and the strength of the in-transit $H\alpha$ signal. The outlier in this case is the data from 2015 August 4 which show both the strongest $H\alpha$ absorption and the highest stellar activity level. If the absorption signal arises in the planetary atmosphere, this reveals a potential stellar activity threshold below which the ionizing flux from the star is not high enough to create large $H\alpha$ transit depths. This should be investigated further with future transits and simultaneous UV measurements of the stellar activity level.
2. We explored detailed simulations of the $H\alpha$ contrast effect for HD 189733 b. We find that large facular/plage coverage fractions of $\gtrsim 5\%$ – 10% and very strong facular/plage core emission strengths of $q_{\text{fac}} \sim 4$ are required to reproduce the observed $H\alpha$ observations. Furthermore, these facular/plage regions must be concentrated very close to the transit chord of the planet. Spots and filaments do not have a significant effect on the $H\alpha$ contrast spectrum.
3. Due to the specificity of the contrast parameters required to reproduce the measured $W_{H\alpha}$ values, combined with the natural explanation of absorption in the thermosphere (Christie et al. 2013), we favor a planetary atmospheric origin for the $H\alpha$ transmission spectra. A similar argument can be made for interpreting the $v_{H\alpha}$ measurements. However, detailed models of active regions on active stars such as HD 189733 are needed to understand whether the necessary contrast parameters are reasonable.
4. We have also explored the velocity centroids of the measured $H\alpha$ transmission spectra using models of planetary rotation. We find that planetary rotational velocities of ~ 9 – 12 km s $^{-1}$ are able to produce in-transit $v_{H\alpha}$ values similar to those from the 2015 August 4 transit. These large velocities are representative of dynamics in the very extended atmosphere and do not necessarily suggest that the planet is rotating faster than the synchronous rate. These models demonstrate that large atmospheric velocities can produce the small observed $v_{H\alpha}$ values and that they do not need to originate on the stellar surface. However, there is no consistent velocity pattern across epochs so the results of the rotation models cannot be broadly applied. Further short-cadence transits at very high S/N are needed to test these ideas.

Future and current planet hunting missions, such as the *Transiting Exoplanet Survey Satellite* and the ground-based Kilodegree Extremely Little Telescope (KELT Pepper et al. 2007) and the Multi-site All-Sky CAmERA (MASCARA Talens et al. 2017), have detected and will detect many hot

planets transiting relatively bright stars. This will significantly increase the number of objects for which short-cadence, high-resolution optical transmission spectroscopy can be performed with 4 m or 10 m class telescopes. In addition, 30 m class telescopes will be able to perform similar observations on much fainter systems. Stars with high activity levels should be targeted as comparison cases with HD 189733 b. Indeed, active stars may be the only systems with hot planets exhibiting $H\alpha$ absorption in their extended atmospheres (Christie et al. 2013). These systems will also act as testbeds for disentangling the contrast effect from true planetary absorption.

Ground-based $H\alpha$ observations of the extended atmospheres of hot planets offers a complementary alternative to the exospheric *Hubble Space Telescope* (*HST*) Ly α observations (Vidal-Madjar et al. 2003, 2013; Lecavelier des Etangs et al. 2010, 2012; Bourrier et al. 2013; Kulow et al. 2014; Ehrenreich et al. 2015). While the $H\alpha$ observations do not probe the escaping exosphere, this ground-based approach may become the best option for measuring the base of evaporative flows due to the impending loss of *HST* and its spectroscopic UV capabilities. It is also critical to develop ground-based transmission spectrum programs in order to plan for and complement future space missions, such as the *Large UV/ Optical/IR Surveyor* (*LUVOIR*). HD 189733 is a benchmark for testing the usefulness of the $H\alpha$ diagnostic and the relationship between stellar activity and the planetary thermosphere. It is thus important to further investigate the observed HD 189733 signals, along with any future detections, to determine the origin of the $H\alpha$ signal and strengthen or repudiate the arguments presented here.

We thank the referee for his/her critique of this manuscript, which helped improve the clarity and style. Some of the data presented herein were obtained at the W.M. Keck Observatory from telescope time allocated to the National Aeronautics and Space Administration through the agency's scientific partnership with the California Institute of Technology and the University of California. This work was supported by a NASA Keck PI Data Award, administered by the NASA Exoplanet Science Institute. The Observatory was made possible by the generous financial support of the W.M. Keck Foundation. The authors wish to recognize and acknowledge the very significant cultural role and reverence that the summit of Maunakea has always had within the indigenous Hawaiian community. We are most fortunate to have the opportunity to conduct observations from this mountain. A.G.J. is supported by NASA Exoplanet Research Program grant 14-XRP14 2-0090 to the University of Nebraska-Kearney. This work was completed with support from the National Science Foundation through Astronomy and Astrophysics Research Grant AST-1313268 (PI: S.R.). This work has made use of NASA's Astrophysics Data System.

References

- Ahn, K., Chae, J., Cho, K.-S., et al. 2014, *SoPh*, **289**, 4117
 Aigrain, S., Pont, F., & Zucker, S. 2012, *MNRAS*, **419**, 3147
 Andersen, J. M., & Korhonen, H. 2015, *MNRAS*, **448**, 3053
 Astudillo-Defru, N., & Rojo, P. 2013, *A&A*, **557**, 56
 Barnes, J. R., Haswell, C. A., Staab, D., & Anglada-Escudé, G. 2016, *MNRAS*, **462**, 1012
 Ben-Jaffel, L., & Ballester, G. E. 2013, *A&A*, **553**, A52
 Berdyugina, S. V. 2005, *LRSP*, **2**, 8
 Berta, Z. K., Charbonneau, D., Bean, J., et al. 2011, *ApJ*, **736**, 12

- Boisse, I., Moutou, C., Vidal-Madjar, A., et al. 2009, *A&A*, 495, 959
- Bouchy, F., Udry, S., Mayor, M., et al. 2005, *A&A*, 444, L15
- Bourrier, V., Lecavelier des Etangs, A., Dupuy, H., et al. 2013, *A&A*, 551, A63
- Boyajian, T., von Braun, K., Feinden, G. A., et al. 2015, *MNRAS*, 447, 846
- Broggi, M., de Kok, R. J., Albrecht, S., et al. 2016, *ApJ*, 817, 106
- Cauley, P. W., Redfield, S., Jensen, A. G., et al. 2015, *ApJ*, 810, 13
- Cauley, P. W., Redfield, S., Jensen, A. G., & Barman, T. 2016, *AJ*, 152, 20
- Cauley, P. W., Redfield, S., & Jensen, A. G. 2017, *AJ*, 153, 185
- Christie, D., Arras, P., & Li, Z.-Y. 2013, *ApJ*, 772, 144
- Collier Cameron, A., Bruce, V. A., Miller, G. R. M., Triaud, A. H. M. J., & Queloz, D. 2010, *MNRAS*, 403, 151
- Cuntz, M., Saar, S. H., & Musielak, Z. E. 2000, *ApJ*, 533, L151
- Czesla, S., Klocová, T., Khalafinejad, S., Wolter, U., & Schmitt, J. H. M. M. 2015, *A&A*, 582, A51
- Dekker, H., D'Odorico, S., Kaufer, A., Delabre, B., & Kotzlowski, H. 2000, *Proc. SPIE*, 4008, 534
- Deng, N., Tritschler, A., Jing, J., et al. 2013, *ApJ*, 769, 112
- Di Gloria, E., Snellen, I. A. G., & Albrecht, S. 2015, *A&A*, 580, A84
- Draine, B. T. 2011, *Physics of the Interstellar and Intergalactic Medium* (Princeton, NJ: Princeton Univ. Press)
- Dumusque, X., Boisse, I., & Santos, N. C. 2014, *ApJ*, 796, 132
- Ehrenreich, D., Bourrier, V., Bonfils, X., et al. 2012, *A&A*, 547, 18
- Ehrenreich, D., Bourrier, V., Wheatley, P. J., et al. 2015, *Natur*, 522, 459
- Eker, Z., Brandt, P. N., Hanslmeier, A., et al. 2003, *A&A*, 404, 1107
- Fares, R., Donati, J.-F., Moutou, C., et al. 2010, *MNRAS*, 406, 409
- Fossati, L., Haswell, C. A., Froning, C. S., et al. 2010, *ApJ*, 714, L222
- Fossati, L., Ingrassia, S., & Lanza 2015, *ApJ*, 812, 35
- Foukal, P. 1998, *ApJ*, 500, 958
- France, K., Parke Loyd, R. O., Youngblood, A., et al. 2016, *ApJ*, 820, 89
- Giguere, M. J., Fischer, D. A., Zhang, C. X. Y., et al. 2016, *ApJ*, 824, 150
- Gray, R. O., & Corbally, C. J. 1994, *AJ*, 107, 742
- Hansteen, V., Carlsson, M., & Gudiksen, B. 2007, in *ASP Conf. Ser.* 368, *The Physics of the Chromospheric Plasmas*, ed. P. Heinzel, I. Dorotović, & R. J. Rutten (San Francisco, CA: ASP), 107
- Hartman, J. D. 2010, *ApJ*, 717, L138
- Heinzel, P., & Anzer, U. 2006, *ApJ*, 643, L65
- Herrero, E., Ribas, I., Jordi, C., et al. 2016, *A&A*, 586, A131
- Hestroffer, D., & Magnan, C. 1998, *A&A*, 333, 338
- Husser, T.-O., Wende-von Berg, S., Dreizler, S., et al. 2013, *A&A*, 553, A6
- Isaacson, H., & Fischer, D. 2010, *ApJ*, 725, 875
- Jensen, A. G., Redfield, S., Endl, M., et al. 2012, *ApJ*, 751, 86
- Johns-Krull, C. M., Hawley, S. L., Basri, G., & Valenti, J. A. 1997, *ApJS*, 112, 221
- Kausch, W., Noll, S., Smette, A., et al. 2014, *ASPC*, 485, 403
- Khalafinejad, S., von Essen, C., Hoeijmakers, H. J., et al. 2017, *A&A*, 598, A131
- Khodachenko, M. L., Shaikhislamov, I. F., Lammer, H., & Prokopov, P. A. 2016, *ApJ*, 813, 50
- Kirk, J., Wheatley, P. J., Loudon, T., et al. 2016, *MNRAS*, 463, 2922
- Kuckein, C., Verma, M., & Denker, C. 2016, *A&A*, 589, A84
- Kulow, J. R., France, K., Linsky, J., & Loyd, R. O. P. 2014, *ApJ*, 786, 132
- Lai, D., Helling, Ch., & van den Heuvel, E. P. J. 2010, *ApJ*, 721, 923
- Lanza, A. F. 2009, *A&A*, 505, 339
- Lanza, A. F. 2014, *A&A*, 572, L6
- Lanza, A. F., Aigrain, S., Messina, S., et al. 2009, *A&A*, 506, 255
- Lanza, A. F., Boisse, I., Bouchy, F., et al. 2011, *A&A*, 533, A44
- Lecavelier des Etangs, A., Bourrier, A., Wheatley, P. J., et al. 2012, *A&A*, 543, L4
- Lecavelier des Etangs, A., Ehrenreich, D., Vidal-Madjar, A., et al. 2010, *A&A*, 514, A72
- Leenaarts, J., Carlsson, M., & Rouppe van der Voort, L. 2012, *ApJ*, 749, 136
- Llama, J., & Shkolnik, E. L. 2015, *ApJ*, 802, 41
- Llama, J., Vidotto, A. A., Jardine, M., et al. 2013, *MNRAS*, 436, 2179
- Llama, J., Wood, K., Jardine, M., et al. 2011, *MNRAS*, 416, L41
- Lockwood, G. W., Skiff, B. A., Henry, G. W., et al. 2007, *ApJSS*, 171, 260
- Logis, C., & Fischer, D. 2010, in *Exoplanets*, ed. S. Seager (Tucson, AZ: Univ. Arizona Press), 27
- Louden, T., & Wheatley, P. J. 2015, *ApJL*, 814, L24
- Matsakos, T., Uribe, A., & Königl, A. 2015, *A&A*, 578, A6
- Mayor, M., Pepe, F., Queloz, D., et al. 2003, *Msngr*, 114, 20
- Menou, K., & Rauscher, E. 2010, *ApJ*, 713, 1174
- Meunier, N., Desort, M., & Lagrange, A.-M. 2010a, *A&A*, 512, A39
- Meunier, N., Lagrange, A.-M., & Desort, M. 2010b, *A&A*, 519, A66
- Miller, B. P., Gallo, E., Wright, J. T., & Pearson, E. G. 2015, *ApJ*, 799, 163
- Miller-Ricci Kempton, E., & Rauscher, E. 2012, *ApJ*, 751, 117
- Murray-Clay, R. A., Chiang, E. I., & Murray, N. 2009, *ApJ*, 693, 23
- Oshagh, M., Santos, N. C., Ehrenreich, D., et al. 2014, *A&A*, 568, A99
- Owen, J., & Adams, F. C. 2016, *MNRAS*, 456, 3053
- Owen, J. E., & Jackson, A. P. 2012, *MNRAS*, 425, 2931
- Pepper, J., Pogge, R. W., DePoy, D. L., et al. 2007, *PASP*, 119, 923
- Pillitteri, I., Maggio, A., Micela, G., et al. 2015, *ApJ*, 805, 52
- Pont, F., Sing, D. K., Gibson, N. P., et al. 2013, *MNRAS*, 432, 2917
- Poppenhaeger, K., & Wolk, S. J. 2014, *A&A*, 565, 1
- Rackham, B., Espinoza, N., Apai, D., et al. 2017, *ApJ*, 834, 151
- Rauscher, E., & Kempton, E. M. R. 2014, *ApJ*, 790, 79
- Rauscher, E., & Menou, K. 2010, *ApJ*, 714, 1334
- Redfield, S., Endl, M., Cochran, W. D., & Koesterke, L. 2008, *ApJ*, 673, L87
- Saar, S. H., & Donahue, R. A. 1997, *ApJ*, 485, 319
- Salz, M., Czesla, S., Schneider, P. C., & Schmitt, J. H. M. M. 2016, *A&A*, 586, 75
- Sanchis-Ojeda, R., & Winn, J. N. 2011, *ApJ*, 743, 61
- Shapiro, A. I., Solanki, S. K., Krivova, N. A., et al. 2015, *A&A*, 569, A38
- Shkolnik, E., Bohlender, D. A., Walker, G. A. H., & Collier Cameron, A. 2008, *ApJ*, 676, 628
- Showman, A., & Guillot, A. P. 2002, *A&A*, 385, 166
- Showman, A. P., Cooper, C. S., Fortney, J. J., & Marley, M. S. 2008, *ApJ*, 682, 559
- Showman, A. P., Fortney, J. J., Lian, Y., et al. 2009, *ApJ*, 699, 564
- Sing, D. K., Pont, F., Aigrain, S., et al. 2011, *MNRAS*, 416, 1443
- Snellen, I. A. G., Brandl, B. R., de Kok, R. J., et al. 2014, *Natur*, 509, 63
- Snellen, I. A. G., de Kok, R. J., de Mooij, E. J. W., & Albrecht, S. 2010, *Natur*, 465, 1049
- Strugarek, A., Brun, A. S., Matt, S. P., & Réville, V. 2014, *ApJ*, 795, 86
- Talens, G. J. J., Spronck, J. F. P., Lesage, A.-L., et al. 2017, *A&A*, in press
- Torres, G., Winn, J. N., & Holman, M. J. 2008, *ApJ*, 677, 1324
- Turner, J. D., Christie, D., Arras, P., Johnson, R. E., & Schmidt, C. 2016, *MNRAS*, 458, 3880
- Valenti, J., & Fischer, D. 2005, *ApJS*, 159, 141
- Vecchio, A., Laurenza, M., Meduri, D., et al. 2012, *ApJ*, 749, 27
- Vidal-Madjar, A., Huitson, C. M., Bourrier, V., et al. 2013, *A&A*, 560, 54
- Vidal-Madjar, A., Lecavelier des Etangs, A., Désert, J.-M., et al. 2003, *Natur*, 422, 143
- Vidotto, A. A., Jardine, M., & Helling, Ch. 2011, *MNRAS*, 414, 1573
- Vogt, S. S., Allen, S. L., Bigelow, B. C., et al. 1994, *Proc. SPIE*, 2198, 362
- Winn, J. N., Johnson, J. A., Marcy, G. W., et al. 2006, *ApJ*, 653, 69
- Worden, J. R., White, O. R., & Woods, T. N. 1998, *ApJ*, 496, 998
- Wright, J. T., Marcy, G. W., Butler, R. P., & Vogt, S. S. 2004, *ApJS*, 152, 261
- Wytenbach, A., Ehrenreich, D., Lovis, C., Udry, S., & Pepe, F. 2015, *A&A*, 577, A62
- Xu, Y., Cao, W., Ding, M., et al. 2016, *ApJ*, 819, 89